CME Article

Recent Advances in 3D Time-Resolved Contrast-Enhanced MR Angiography

CME

Stephen J. Riederer, PhD,[1] Clifton R. Haider, PhD,[2] Eric A. Borisch, MS,[1] Paul T. Weavers, PhD,[1] and Phillip M. Young, MD[3]

This article is accredited as a journal-based CME activity.
If you wish to receive credit for this activity, please refer to the website: www.wileyhealthlearning.com/jmri

ACCREDITATION AND DESIGNATION STATEMENT

Blackwell Futura Media Services designates this journal based CME activity for a maximum of 1 *AMA PRA Category 1 Credit*™. Physicians should only claim credit commensurate with the extent of their participation in the activity.
Blackwell Futura Media Services is accredited by the Accreditation Council for Continuing Medical Education to provide continuing medical education for physicians.

EDUCATIONAL OBJECTIVES

Upon completion of this educational activity, participants will be better able to:

1. Recognize the technical factors contributing to the marked improvement in the spatiotemporal resolution of time-resolved contrast-enhanced MR angiography over the last two decades.
2. Identify the range of clinical applications of time-resolved contrast-enhanced MR angiography.

ACTIVITY DISCLOSURES

No commercial support has been accepted related to the development or publication of this activity.

Faculty Disclosures:

Editor-in-Chief: Mark E. Schweitzer, MD, has no relevant financial relationships to disclose.

CME Editor: Scott B. Reeder, MD, PhD, discloses support from General Electric, and founder's equity in Morpheus Medical.

CME Committee: Shreyas Vasanawala, MD, PhD, discloses research collaboration with GE Healthcare and co-founder equity in Morpheus Medical.

Scott K. Nagle, MD, PhD, discloses consulting fees from Vertex Pharmaceuticals for consulting in design of cystic fibrosis clinical trials involving imaging; and departmental research support from General Electric for evaluation of products and development.

Mustafa R. Bashir, MD, discloses research support from Siemens Healthcare and Bayer Healthcare.

Tim Leiner, MD, PhD, discloses research support grant funding from Bracco, S.p.A., Philips Healthcare, and Bayer Healthcare.

Bonnie Joe, MD, PhD, has no relevant financial relationships to disclose.

Authors: Stephen J. Riederer, Ph.D., Clifton R. Haider, Ph.D., and Paul T. Weavers, Ph.D., disclose patent license royalty from GE Healthcare. Eric A. Borisch M.S. and Phillip M. Young, M.D. have no relevant financial relationships to disclose.

This manuscript underwent peer review in line with the standards of editorial integrity and publication ethics maintained by Journal of Magnetic Resonance Imaging. The peer reviewers have no relevant financial relationships. The peer review process for Journal of Magnetic Resonance Imaging is double-blinded. As such, the identities of the reviewers are not disclosed in line with the standard accepted practices of medical journal peer review.
Conflicts of interest have been identified and resolved in accordance with Blackwell Futura Media Services' Policy on Activity Disclosure and Conflict of Interest.

INSTRUCTIONS ON RECEIVING CREDIT

For information on applicability and acceptance of CME credit for this activity, please consult your professional licensing board.
This activity is designed to be completed within an hour; physicians should claim only those credits that reflect the time actually spent in the activity. To successfully earn credit, participants must complete the activity during the valid credit period.
Follow these steps to earn credit:

- Log on to www.wileyhealthlearning.com/jmri
- Read the target audience, educational objectives, and activity disclosures.
- Read the article in print or online format.
- Reflect on the article.
- Access the CME Exam, and choose the best answer to each question.
- Complete the required evaluation component of the activity.

This activity will be available for CME credit for twelve months following its publication date. At that time, it will be reviewed and potentially updated and extended for an additional period.

[1]Mayo Clinic, MR Laboratory, Rochester, Minnesota, USA.
[2]Mayo Clinic, SPPDG, Rochester, Minnesota, USA.
[3]Mayo Clinic, Radiology, Rochester, Minnesota, USA.

Additional Supporting Information may be found in the online version of this article.

*Address reprint requests to: S.J.R., Mayo Clinic, MR Laboratory, 200 First St., S.W., Rochester, MN 55905. E-mail: riederer@mayo.edu

Received Aug 19, 2014; Accepted Dec 31, 2014
DOI 10.1002/jmri.24880
View this article online at wileyonlinelibrary.com.

Contrast-enhanced magnetic resonance angiography (CE-MRA) was first introduced for clinical studies approximately 20 years ago. Early work provided 3–4 mm spatial resolution with acquisition times in the 30-second range. Since that time there has been continuing effort to provide improved spatial resolution with reduced acquisition time, allowing high resolution 3D time-resolved studies. The purpose of this work is to describe how this has been accomplished. Specific technical enablers have been: improved gradients allowing reduced repetition times, improved *k*-space sampling and reconstruction methods, parallel acquisition, particularly in two directions, and improved and higher count receiver coil arrays. These have collectively made high-resolution time-resolved studies readily available for many anatomic regions. Depending on the application, ~1 mm isotropic resolution is now possible with frame times of several seconds. Clinical applications of time-resolved CE-MRA are briefly reviewed.

Key Words: MRA; contrast-enhanced MRA; time-resolved studies; fast imaging; parallel imaging

J. Magn. Reson. Imaging 2015;42:3–22.

There are many clinical situations in which time-resolved contrast-enhanced magnetic resonance angiography (CE-MRA) may be valuable. The multiple images of a time-resolved acquisition may improve diagnostic accuracy by depicting arterial anatomy without venous contamination in cerebral, extremity, and renal and visceral artery imaging. In some cases, timing a single-phase CE-MRA scan may be difficult, such as in the setting of inflow disease or hyperemia causing asymmetric flow in the lower extremities, or because of the rapid transit time and small contrast bolus volume in children. Time-resolved imaging may be useful in visualizing unusual vascular flow patterns, such as retrograde filling of a vessel distal to an occlusion.

One of the initial demonstrations of 3D CE-MRA was Prince's work in the mid-1990s (1), which showed the ability to image the vasculature in 3D but with coarse spatial resolution. Shortly thereafter, there were efforts to simultaneously improve the speed of acquisition and provide improved spatial resolution. In the quest to perform time-resolved imaging one is confronted by a fundamental tradeoff in MRI between acquisition time and spatial resolution. In general, unless some separate physics principle is newly applied or the underlying pulse sequence is altered, reduction of the acquisition time in MRI must be accompanied by a reduction in the spatial resolution.

In the last 20 years the discovery, exploitation, and implementation of various MRI physics principles and the development of improved MRI hardware has radically altered the temporal vs. spatial resolution tradeoff of CE-MRA of the mid-1990s, allowing more than an order of magnitude reduction in the acquisition time. In numerous vascular territories time-resolved CE-MRA is now possible with spatial resolution superior to that which was previously available only in single phase imaging. In this article we provide an overview of this evolution, review methods contributing to this, and describe applications. This work can be considered a companion to recent review articles that have covered parallel imaging (2), MRI temporal acceleration techniques (3), and time-resolved angiography (4). Noncontrast-enhanced (NCE) MRA, as reviewed recently (5), constitutes a significant subfield of its own and is beyond the scope of this article. As the name implies, NCE-MRA methods do not require contrast administration. They generally depend on pulsatile or steady arterial blood flow, are subject to signal loss from multiple radiofrequency (RF) excitations, and for various reasons require acquisition times of minutes. For CE-MRA these first issues are less problematic, and the short T_1 relaxation time of enhanced blood allows significantly shorter acquisition times.

EVOLUTION OF TIME-RESOLVED MRA

Perhaps the principal take-home point of this review article is that multiple technical advances over the last 20 years have allowed significant, indeed radical, reduction in acquisition time, providing marked improvement in the spatial-temporal resolution of time-resolved 3D CE-MRA. In this section we trace the evolution in performance by selecting a specific anatomic region, the vasculature of the calves, and observing how performance has improved. Table 1 shows this evolution, and is explained as follows.

Assume that bilateral CE-MRA of the calves is to be performed with 3D Fourier Transform (3DFT) acquisition in coronal format: frequency encoding in the superior/inferior (S/I) direction, phase encoding left/right (L/R), and slice encoding anterior/posterior (A/P), with corresponding field-of-view (FOV) of 400 × 320 × 132 mm^3. Several possible Y × Z spatial resolutions within the axial plane are shown heading the columns of Table 1, resolution improving left to right. The absolute $N_Y \times N_Z$ sampling resolution is shown in the third row. For the typical gradient echo pulse sequence used in CE-MRA with one phase encoding measurement or "view" sampled per repetition interval TR, the number of repetitions used for 3DFT acquisition is $N_Y \times N_Z$. However, for all entries in this table it is assumed that the corners of k_Y-k_Z space are not sampled (6), providing more isotropic resolution within the Y × Z plane, allowing a 25% reduction in this $N_Y \times N_Z$ product. Shown in the fourth row is the resultant total number of necessary repetitions. The acquisition time is equal to this number multiplied by TR.

Just as moving left to right in Table 1 corresponds to improved spatial resolution, moving downward in the table from the fifth row on corresponds to progressive reduction in acquisition time, with entries for specific repetition times (TR, in msec) shown within groupings for specific acceleration factors R = 1 (no acceleration), 2, 4, and 10, where R is the reduction in scan time allowed by parallel acquisition. The evolution of performance corresponds to migration from the top left to

Table 1
Evolution of Spatial Resolution and Acquisition Time for CE-MRA of the Calves

Spatial Resolution (Y × Z)		3.35 × 4.13 mm^2	2.50 × 2.06 mm^2	1.67 × 1.38 mm^2	1.00 × 1.00 mm^2
Figure		1a, e	1b, f	1c, g	1d, h
Sampling Resolution (Y × Z)		96 × 32	128 × 64	192 × 96	320 × 132
Total No. Views Without *k*-Space Corners		2304	6144	13824	31680
Times (sec)					
No Acceleration R = 1	TR 14.1	32	87		
	TR 10	23 8.0 / 32	61 21.5 / 86		
	TR 5	11.5	30 10.7 / 43	69 24 / 96	
Acceleration R = 2	TR 10	11.5	30	69	
	TR 5	5.8	15 5.3 / 21	34 12.1 / 48	79 27 / 110
Acceleration R = 4	TR 10	5.7	15	34	79
	TR 5	2.8	7.6 2.7 / 10.7	17 9.6 / 24	39 13.8 / 55
	TR 3	1.7	4.6	10.4 3.6 / 14	23 8.3 / 33
Acceleration R = 10	TR 5	1.1	3.0 1.0 / 4.3	6.9 2.4 / 9.7	15 5.5 / 22
	TR 3	0.7	1.8 0.7 / 2.6	4.1 1.4 / 5.8	9.5 3.3 / 13

References:

Prince, Ref. (7)	Korosec, Ref. (8)	Weiger, Ref (10)
Hu, Ref. (14)	Bonel, Ref. (18)	Haider, Ref. (21)

Columns left to right indicate improved axial spatial resolution. Top rows indicate sampling parameters. Subsequent rows from top to bottom indicate reduced times due to TR reduction and increased acceleration (R) from parallel acquisition. Body of table indicates acquisition time (in sec) for single phase imaging and frame time / temporal footprint (assumed to be 4× frame time) for time-resolved acquisition with view sharing. Assumed field of view is 40 (S/I) × 320 (L/R) × 132 (A/P) mm^3. Images corresponding to the resolutions indicated are presented in Figure 1. TR times are indicated in msec.

the bottom right of the table. Specific entries to be discussed are highlighted in color. Contrast-enhanced MR angiograms which illustrate the various spatial resolution combinations heading the columns are provided in Fig. 1.

As a starting point, the parameters described in Prince's early work in abdominal CE-MRA (7), which used a repetition time of 14.1 msec, are applied here to the calves. As highlighted in the table, this corresponds to an acquisition time of 32 seconds for the

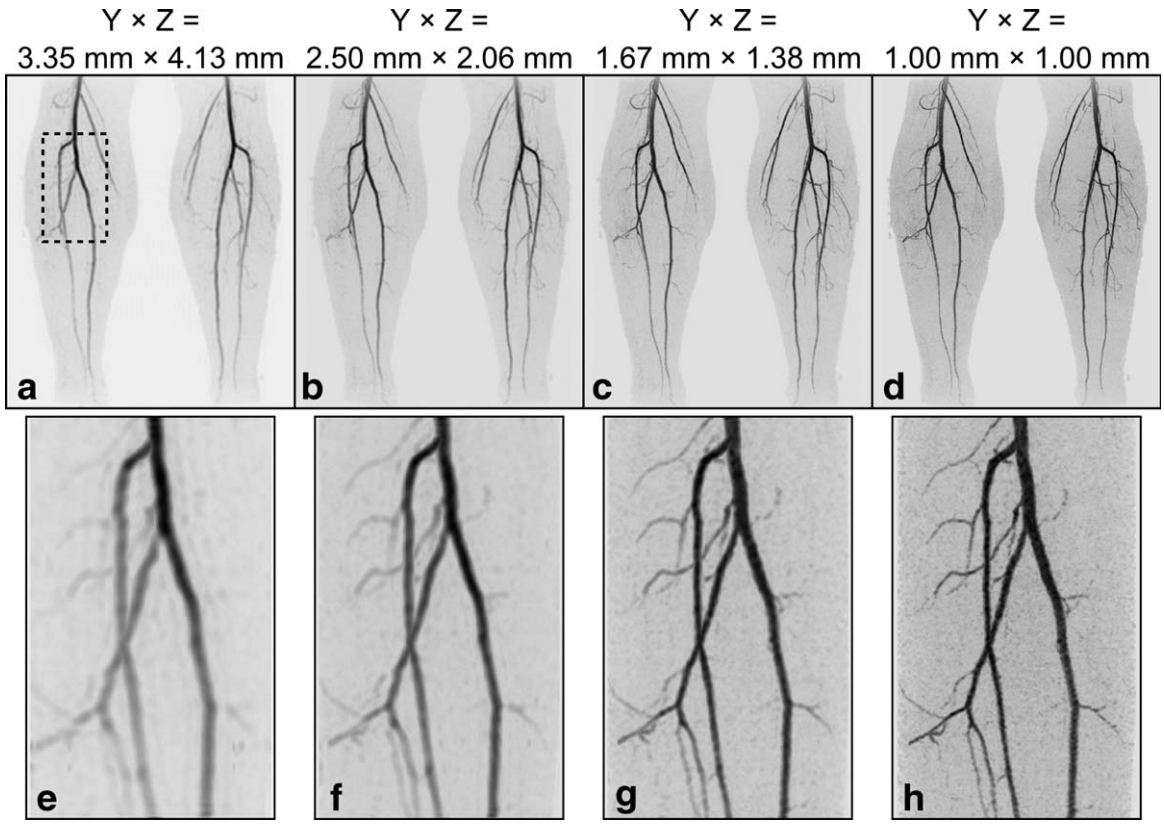

Figure 1. Illustration of the evolution of spatial resolution of CE-MRA. Shown for each resolution is a coronal MIP of the full FOV (**a–d**) and a targeted MIP (**e–h**) at a slight angle of a small region of the right calf (identified in the dashed box in a). The progressions of images from (a–d) and from (e–h) correspond to the progression of axial resolution indicated in the column headings of Table 1.

coarsest spatial resolution considered. After this initial demonstration of CE-MRA, investigators quickly recognized the importance of small TR times for enabling high spatial resolution, and the next row in the table shows results for TR 10 msec.

Shortly after the initial demonstration of 3D CE-MRA the view-sharing TRICKS technique (8) was introduced, also highlighted in Table 1. This permitted a reduced frame time, here shown as 8 seconds, but due to more frequent sampling of central *k*-space caused some increase in temporal footprint (32 sec) vs. single phase imaging (23 sec). Note that the times indicated in the table are based on the parameters shown for each column and row and thus might differ from the values reported within the cited references. A subsequent study of TRICKS (9) for imaging the vasculature of the calves used TR times of 7.8 msec and provided improved performance, i.e. moved the operating point in Table 1 to the right and below that for the highlighted entry.

Another distinct step in the development of contemporary CE-MRA was the incorporation of parallel acquisition. Early work (10–12) used 1D acceleration factor $R=2$, as highlighted in Table 1 for Ref. 10, with the parameters used therein for renal MRA converted to the peripheral vasculature for this presentation. The acquisition speed of these studies also benefited from TR times as low as 5 msec.

3DFT acquisition incorporates phase encoding along two directions, allowing 2D (13) vs. 1D parallel acquisition. An early example of 2D acceleration with $R=4$ for CE-MRA is highlighted (14). In the ensuing years multiple investigators further developed parallel imaging for the periphery (15–17). Highlighted is the work of Bonel et al (18), which used acceleration $R=3$ with the GRAPPA technique (19).

Additional development of 2D acceleration, possibly in combination with other undersampling methods such as partial Fourier acquisition and homodyne reconstruction (20), has allowed net acceleration factors of $R=10\times$ or more (21,22), also highlighted. Effective use of acceleration factors this high requires appropriate receiver coil arrays, as will be discussed.

VIEW SHARING

Virtually all time-resolved methods in 3D CE-MRA use view sharing (23) to provide a frame time shorter than the intrinsic acquisition time for a single image. MRI data are measured in the spatial frequency domain of the image, referred to as "*k*-space," rather than in the image domain itself. Because individual spatial frequencies are measured serially, images can be generated more frequently than the intrinsic acquisition time for sampling all of *k*-space.

Although non-Cartesian implementation is possible, this section assumes 3D Cartesian acquisition, as in the previous section. In this case analysis of *k*-space sampling is facilitated by focusing on the k_Y-k_Z plane.

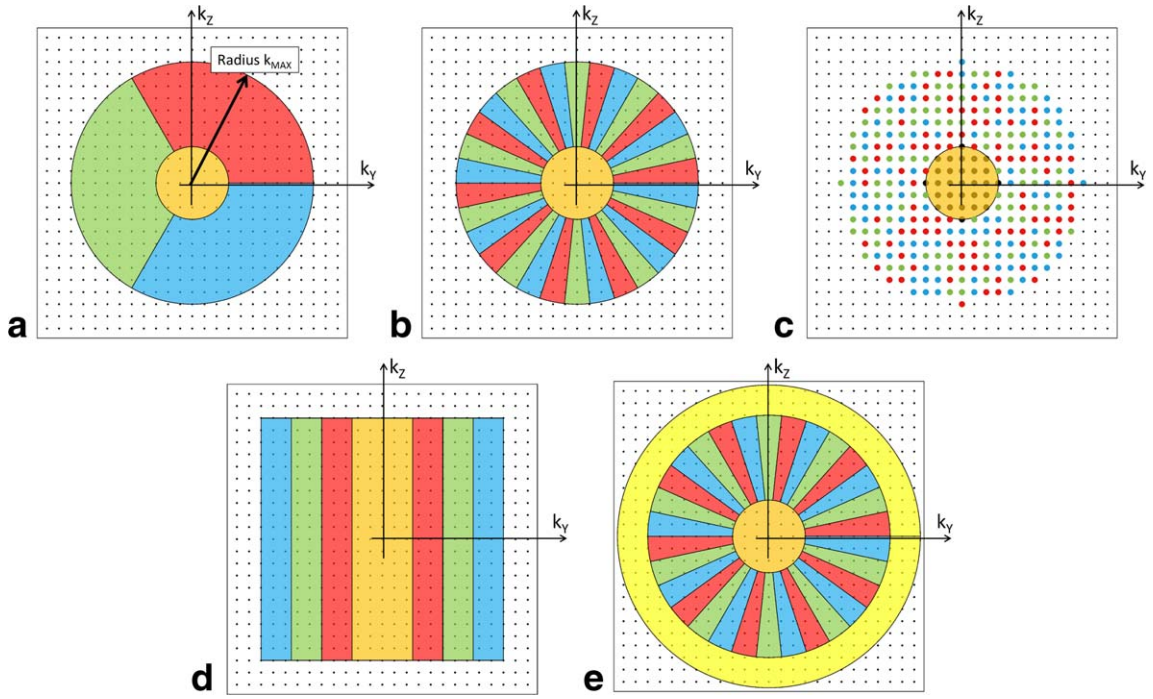

Figure 2. *k*-space sampling methods for view-shared 3D CE-MRA. Shown for (**a–e**) is a plot of k_Y-k_Z space. Contemporary methods generally first identify a central region which encompasses the k_Y-k_Z origin (orange). Next, sampling is defined for peripheral *k*-space, extending outward to some radius, k_{MAX}, and subdivided into groups. One straightforward way for subdividing is to use sectors (a) with three shown here (red, green, blue). To better disperse artifacts when only central *k*-space and a limited number of subsets of peripheral *k*-space are sampled, the points among groups are more interspersed. With the CAPR method (b) this is done using slender vanes. For even better dispersion peripheral *k*-space can be apportioned into three random-appearing sets (c). For reference the original TRICKS technique used grouping along the k_Y direction (d). For improved spatial resolution one can adjust the acquisition to sample out to larger *k*-radii (e).

All points are located on a rectilinear grid, an individual point (k_Y,k_Z) in this plane is sampled each TR interval, and because sampling along k_X for such a point occurs virtually instantaneously within the several-msec-long echo, effects along k_X can be ignored. Figure 2a schematically shows the possible sampled points of k_Y-k_Z space as well as a central sampling region (orange) and three colored sectors in peripheral *k*-space (red, green, blue) extending out to some maximum radius k_{MAX}. As assumed in Table 1, the corners of k_Y-k_Z space are not sampled. Time-resolved 3D acquisition is performed by sampling the points within each region according to some prescribed time order and frequency.

The use of sectors in Fig. 2a allows clear distinction of individual subsets of peripheral *k*-space points. With contemporary time-resolved methods alternative decompositions of peripheral *k*-space are generally used. For example, the "Cartesian Acquisition with Projection Reconstruction-like sampling" (CAPR) technique (24) uses interleaved sets of vanes (Fig. 2b). This tends to better disburse any artifacts due to undersampling vs. the approach in Fig. 2a. The "Time-resolved angiography With Stochastic Trajectories" (TWIST) method (25) takes this a step further by placing peripheral *k*-space points into interleaved spiral trajectories based on their distance from the k_Y-k_Z origin. This yields a random appearance as depicted in Fig. 2c. As a reference the original TRICKS technique (8) used subsets that were progressively located along the $\pm k_Y$ direction (Fig. 2d). Other decompositions are possible, such as "Differential Subsampling with Cartesian Ordering" (DISCO) (26), which has a pattern similar to Fig. 2c. Once all regions are defined the acquisition proceeds as follows.

Figure 3 shows how view-shared methods are implemented in CE-MRA. As a reference, Fig. 3a shows the typical timing of a CE-MRA exam. Contrast material is injected intravenously and after some delay appears in the targeted arterial vasculature. A short time later the contrast-enhanced blood appears in the companion venous vasculature. The injection-to-arrival time and arterial-venous delay time depend on the arterial vasculature under study and have high patient-to-patient variability. Typical ranges are 5 to 50 seconds for the former and 2 to 15 seconds for the latter (27,28). The challenge of CE-MRA is to acquire a high spatial resolution image timed to the arterial phase with negligible, potentially confounding enhancement of the companion veins.

A progression of acquisition strategies is shown in the remainder of the figure. In Fig. 3b the "Acq" line shows how the regions of k_Y-k_Z space of any of the methods in Fig. 2a–d might be sampled over time. For purposes of discussion, suppose that each colored block is 8 seconds long. The corresponding "Recon" lines show how the acquired data are selected to reconstruct images. Image I1 is reconstructed from

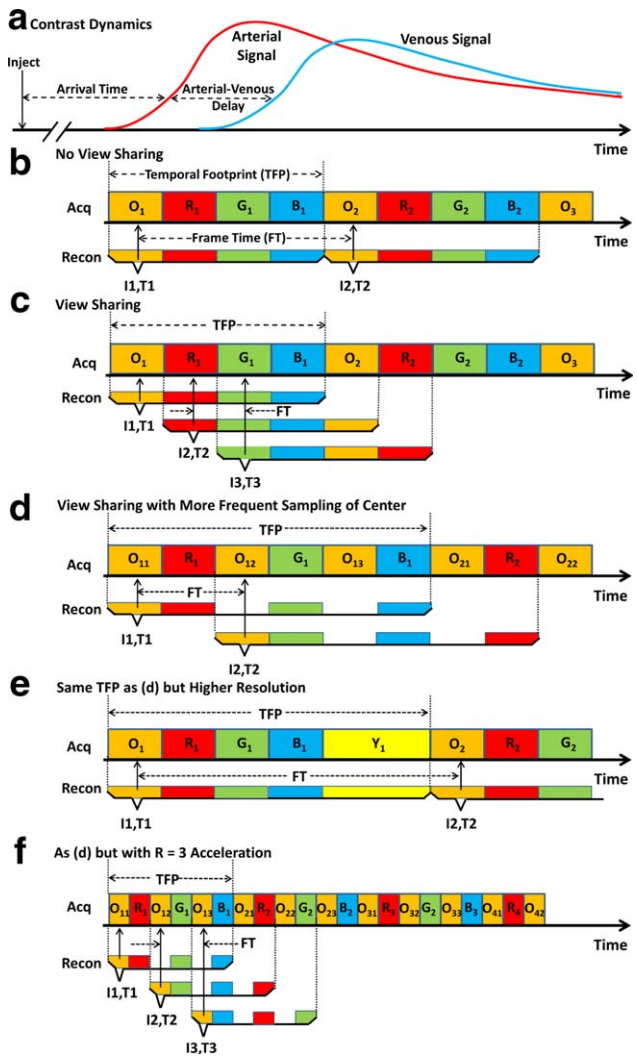

Figure 3. View-sharing temporal readouts. **a:** Typical timing in CE-MRA. After intravenous contrast injection there is some patient-specific arrival time delay after which contrast-enhanced blood arrives at the target artery. After some subsequent arterial-venous delay the companion veins enhance. **b–d,f:** The temporal playout using any of the sampling methods of Fig. 2a–d. (b) Temporal sampling of k_Y-k_Z space with no view sharing. After all desired samples are first acquired (all four colored groups in the Acq line), those data are used for reconstruction, and the process is repeated. Frame time (FT) matches temporal footprint (TFP). (c) Simple view sharing. Same acquisition as (b) but more frequent reconstruction with each reconstruction using the designated colored blocks within the corresponding bracket. FT is reduced 4× vs. (b) but TFP remains the same. d: Acquisition with 3× increased frequency of sampling central (orange) *k*-space and view sharing. Reconstruction is done in synchrony with sampling central *k*-space. FT is half that of (b) but TFP is increased by 50%. **e:** Alternative acquisition with same TFP as (d) but with improved spatial resolution and increased FT vs. (b,d). **f:** Temporal sampling of all *k*-space sectors assuming acceleration factor R = 3. Note that image I3 and I4 (not shown) are temporally well aligned with peak arterial signal in (a). Also the temporal footprint has been reduced 3× vs. (d) so that almost all *k*-space sampling is performed prior to venous enhancement.

the colored data selected within the corresponding bracket, and it is ascribed to time T_1, designated with the short vertical arrow. The simplest way to generate a time-resolved image series is to repeat this process multiple times as in Fig. 3b, yielding Image I2 at time T_2, etc. In this case the time between successive images, or the frame time (FT), is equal to the time required to sample all of k_Y-k_Z space, defined as the temporal footprint (TFP) (24). Depending on when the sequence is initiated, Image I1 or I2 might or might not capture the arterial phase.

With view sharing (Fig. 3c) it is recognized that image reconstruction can be done more frequently than the time required to sample all of *k*-space. As seen, the data acquisition is identical to Fig. 3b, and Image I1 of Fig. 3c is formed identically to Fig. 3b). However, Image I2 is reconstructed after the next subregion of *k*-space has been sampled (O2). Samplings R1, G1, B1 are "shared" for images I1 and I2. Because the frame time in Fig. 3c is four times shorter than in Fig. 3b, one might think that this method would be more likely to capture the arterial phase. However, the overall appearance of the image is dictated by the sampling of the orange central *k*-space region. Because the frequency of sampling this region has not changed vs. Fig. 3b, the performance is not markedly improved. Expressed another way, because images such as I2 and I3 share their central *k*-space sampling (O2 in this case), they provide redundant information.

View sharing in Cartesian sampling is best exploited if central *k*-space is sampled more frequently than peripheral *k*-space (Fig. 3d). In this case the orange central region is sampled prior to each of the three peripheral regions, and an image is reconstructed corresponding to each of these samplings. Compared to Fig. 3b, the frame time is two times shorter, and because central *k*-space is sampled more frequently than in Fig. 3b, the likelihood of capturing the arterial phase is improved. In fact, in Fig. 3d the central *k*-space sampling O_{12} for image I2 is better aligned temporally with the peak arterial signal in Fig. 3a than the methods in Fig. 3b or c. However, this is done at the expense of the temporal footprint being longer, six intervals now vs. the four of Fig. 3b. If one is willing to allow a temporal footprint this long, an alternative acquisition is one that uses this extra time to sample k_Y-k_Z space even more peripherally to obtain a single phase image with even higher spatial resolution. This is shown in the expanded *k*-space coverage of Fig. 2e and the data acquisition and reconstruction in Fig. 3e. In this case one generally uses some kind of timing method (29,30) to initiate this high-resolution scan with arterial contrast arrival.

Finally, Fig. 3f shows the case when parallel acquisition is applied to the sequence of Fig. 3d. In this example R = 3 is assumed, causing the width of each colored block to be reduced proportionately vs. the previous parts of the figure. Compared to Fig. 3d, the frame time and the temporal footprint are similarly reduced three-fold. Comparison with the contrast enhancement waveforms in Fig. 3a suggests that one

or more images of the accelerated sequence in Fig. 3f will be temporally aligned with the arterial phase. Also, the reduced temporal footprint reduces the sensitivity of the arterial phase image to venous enhancement.

Modern day time-resolved CE-MRA can be performed with acceleration factors R of 2 to 4 being routine, 4 to 6 being common, and 8 to 16 being possible for certain applications. Factors $R > 3$ further compress the temporal playout beyond that shown in Fig. 3f. Rather than use such high acceleration factors solely for reduction of frame time and temporal footprint, some of the advantage can be directed toward improved spatial resolution. That is, sampling of more peripheral *k*-space regions can be incorporated into the sequence while still providing a frame time and temporal footprint smaller than in Fig. 3d. This usage has allowed migration of the operating point in Table 1 both downward (faster) and rightward (improved spatial resolution).

Prior to the advent of parallel acquisition, two other methods used to provide a reduced frame time were keyhole imaging and temporal interpolation. Keyhole imaging (31) repeatedly samples only central *k*-space during the arterial enhancement period, sampling peripheral *k*-space only at the end of the scan. This generally results in blurring, akin to that seen in Fast- (FSE) or Turbo-Spin-Echo (TSE) T_1-weighted sequences (32). In both cases the peripheral *k*-space samples have attenuated magnetization levels, in keyhole from waning contrast enhancement and in FSE/TSE from T_2 decay. Temporal interpolation was used, for example, in the original TRICKS method (8). Rather than representing the object status at the interpolated time, however, temporal interpolation results in a superposition of the object status at both reference times. The advent of acceleration largely obviates both of these methods, and TRICKS can be used with acceleration (33).

In considering the data sorting for the sequences in Figs. 3d and f, one might question which sampling of central *k*-space to use in reconstruction. For example, three samplings (O_{12}, O_{13}, O_{21}) are within the temporal footprint for Image I2. Here, the earliest sampling within each footprint was used for illustration. The specific choice is up to the user; considerations are discussed in Ref. 34. Use of an early sampling can cause artifactual, premature enhancement of vessels, called "anticipation artifact." Use of a late sampling can cause diminished spatial resolution at the leading edge of contrast. Averaging the multiple central samplings blunts the temporal sharpness of only one sampling. Whatever the choice, it is best to maintain it for all images in the series to provide consistent image-to-image portrayal of a changing signal.

Another consideration is the specific time ordering of sampling the phase encoding views within each *k*-space region. This is arbitrary. Typically, elliptical centric (35), some centric-like sampling such as "Contrast-ENhanced Timing-Robust Angiography" (CENTRA) (36), or a combined centric-in/out sampling of central k_Y-k_Z region is employed (37) to preserve temporal sharpness. Similarly, the number of peripheral k_Y-k_Z regions and the relative size of the central vs. peripheral regions are additional variables. Determination of specific values can depend on the application, as studied, for example, in renal imaging (37) or fluoroscopic tracking (38).

ACCELERATION IN 3D CE-MRA

Partial Fourier acquisition is performed in MRI for up to 2-fold reduction in the number of samples in some direction of *k*-space (39) and is noted here as a means for reducing scan time in 3D CE-MRA. In one implementation asymmetric sampling is done in k_Y-k_Z space with zero filling (40). In another (41) the sampled and nonsampled regions in peripheral *k*-space are interleaved and homodyne reconstruction (20) performed. Partial Fourier can also be done along the readout in both Cartesian (40) and radial acquisition (42) for TR reduction.

Parallel acquisition was first described over a decade ago and has been reviewed various times subsequently (eg, Refs. 2, 43, 44). This section presents those aspects important for 3D time-resolved CE-MRA. As discussed in these reviews, the measurement of separate coil sensitivity images or autocalibration lines is necessary for SENSE-like (13,45) and GRAPPA-like (19,46) approaches, respectively. This can be done once, either before or after acquisition of the accelerated, time-resolved datasets, or possibly embedded within the accelerated acquisition itself using approaches such as TSENSE (47) or TGRAPPA (48).

3D CE-MRA imaging of the calves is shown schematically in Fig. 4a. As assumed for Table 1, frequency encoding (X) is S/I, phase encoding (Y) is L/R, and slice encoding (Z) is A/P. As in Fig. 2 the phase encoding (k_Y-k_Z) plane can be isolated for analysis (Fig. 4d). Assume that each open blue circle corresponds to an individual repetition of a reference unaccelerated acquisition. With 3DFT acquisition separate acceleration factors, R_Y and R_Z, can be applied along the respective phase encode directions Y and Z, and the overall acceleration is the product, $R = R_Y \times R_Z$. In k_Y-k_Z space this is implemented by proportionately increasing the sampling distance along the corresponding direction. For example, if the original acquisition in (d) is accelerated by $R_Y = 5.4$ and $R_Z = 2.5$, yielding $R = 13.5$, the resultant sampling pattern corresponds to the orange points shown. This illustrates that: 1) acceleration factors along Y and Z can be different from each other; 2) acceleration factors need not be an integer; and 3) the actual *k*-space points sampled can be different in the accelerated vs. the nonaccelerated scan. An aliased axial subtraction image from one element of a 16-element array used in acquiring such an accelerated CE-MRA scan of the calves is shown in (e), and the unaliased result in (f). The corresponding maximum intensity projection (MIP) image is shown in Supplemental Fig. S1.

Parallel acquisition requires that the MR signal generated during each repetition of the acquisition be

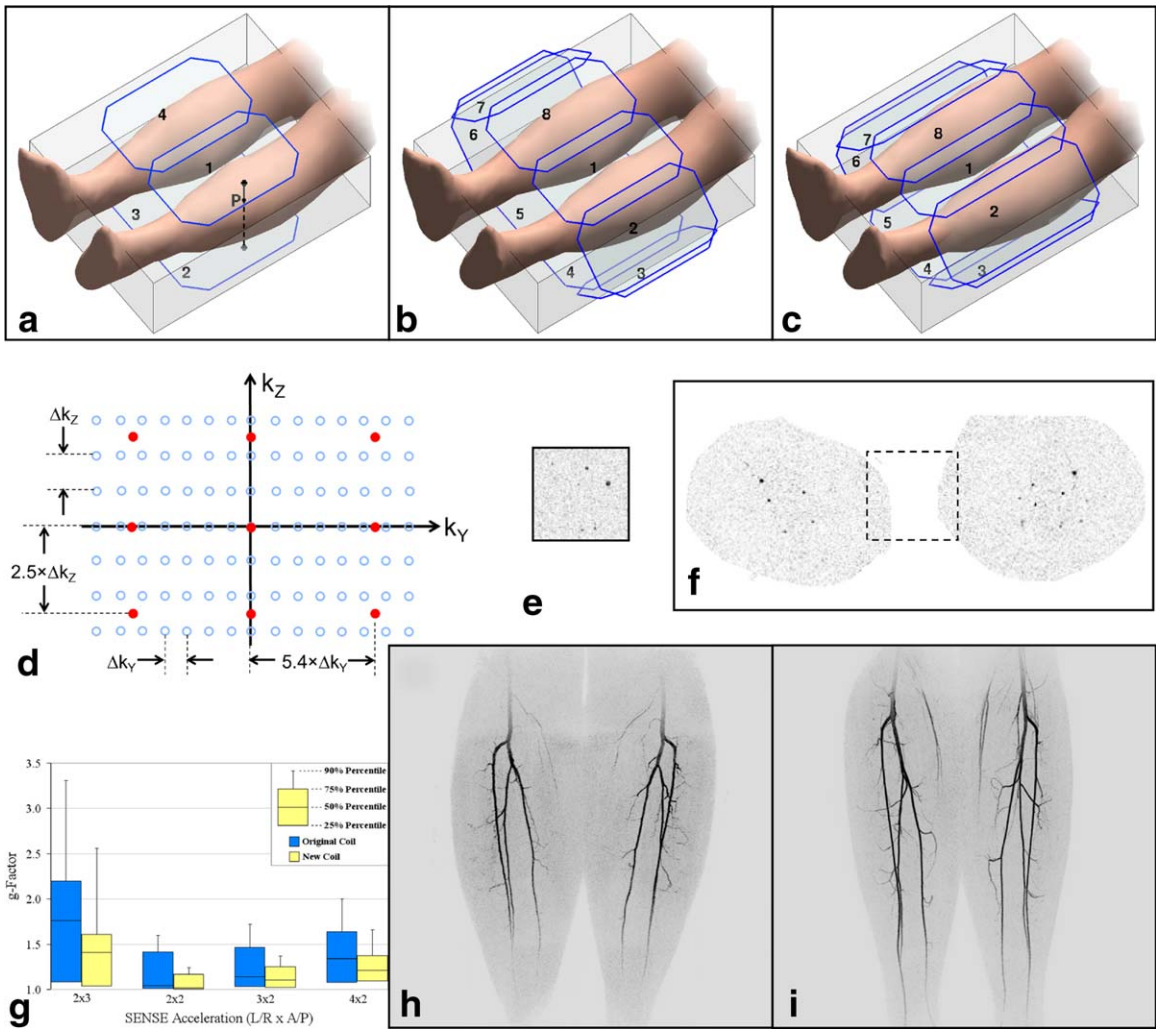

Figure 4. 2D parallel acquisition in CE-MRA. **a:** Schematic of calves with 3D FOV and simple four-element coil. Point P is described in the text. **b:** Similar to (a) but with eight-element coil with all elements of equal area. **c:** Similar to (a,b) but with further adapted coil with more slender anterior and posterior elements (1,4,5,8) and longer elements overall than in (b). **d:** Plot of k_Y-k_Z space with samplings for reference unaccelerated (blue) and accelerated scans (orange). The assumed acceleration is $R_Y \times R_Z = 5.4 \times 2.5 = 13.5$. **e:** Axial aliased image from accelerated 3D CE-MRA exam of the calves using the acceleration of (d). **f:** Unaliased image from same study as (e). The reduced FOV of the accelerated acquisition is shown in the dashed box. **g:** Plot of g-factors of 3D volume of the calves using the receiver coil arrays of (b) (blue) and (c) (yellow) for various acceleration factors. Note the overall reduced g-factors of the latter. **h:** MIP made from CE-MRA exam of calves using coil array of (b) with $R = 7.3$. **i:** MIP made from CE-MRA of calves of different volunteer using coil array of (c) with $R = 8$ (g-i taken from Ref. 21).

simultaneously detected by each element of a multi-element receiver coil. Thus, the receiver coil array is a critical enabler for effective parallel acquisition.

The receiver coil array must meet several technical specifications. In general, the number of coil elements must match or exceed the acceleration factor R. Also, the sizes, positions, and orientations of the coil elements over the FOV must cause the coil sensitivity profiles to be dissimilar from each other. If not, the reconstruction process is prone to severe signal-to-noise ratio (SNR) loss due to mathematically inverting a poorly conditioned matrix. For $R = 2$ SENSE acceleration this is equivalent to solving two equations in two unknowns in which the coefficients of the two equations are nearly identical. The coil sensitivities are analogous to these coefficients. Slight alteration of the two measurements causes major uncertainties in the computed unknowns.

Many coil arrays have been used for parallel acquisition. A progression is illustrated in Fig. 4 for the calves. Consider first the four-element case (a) and point P at the surface of the left calf near Coil 1. As one moves from this point through the calf in the posterior direction toward Coil 2, the sensitivity of Coil 1 to the point diminishes owing to the increased distance, while that of Coil 2 increases because the distance from Coil 2 is decreasing. That is, the sensitivities of Coils 1 and 2 along this Z direction are dissimilar, or more specifically, complementary. Consequently, this coil orientation supports acceleration along Z. Also, Coils 1 and 4 have complementary sensitivities for paths along the L/R direction, supporting

acceleration along Y. This configuration has been used for 2D acceleration with R = 4 (14). This can be extended to an eight-element array (b) in which the elements are wrapped completely around the calves. Acceleration along the Y (L/R) direction is improved vs. (a) because of the laterally placed elements, and the higher coil count allows higher R values.

The degree to which a coil array provides good quality acceleration due its coil elements having dissimilar responses can be assessed mathematically using the "g-factor" (45). This is a mathematical construct based on the sensitivities of all coil elements and defined to have a numerical value of 1 (unity) or higher. A value of 1 indicates perfect response, i.e. no loss of SNR due to the dealiasing process. The higher the value, the greater is the SNR loss. For a specific coil array and acceleration factor R, the g-factor can be computed at every point within the FOV. Figure 4g shows in blue the range of g-factors over the 3D calves volume for various 2D acceleration combinations using the coil shown schematically in (b). Figure 4h is a CE-MRA image of the calves using this coil and an R = 7.3 CE-MRA acquisition. Technical interpretation of these results suggested that the array could be improved if the anterior and posterior elements were adjusted to have a more rapid sensitivity falloff with increased depth in the object and all elements elongated for better S/I coverage. This led to the design of narrower anterior and posterior elements (c), resulting in a different g-factor, shown in the yellow plots in (g), with markedly reduced (improved) values vs. the blue plots. Figure 4i shows a CE-MRA result with the modified coil of (c) acquired with R = 8. In spite of the higher acceleration factor vs. (h), it has higher SNR, consistent with the reduced g-factors.

In the last decade multielement whole-body coil arrays have been developed as described previously (e.g. Refs. 49,50), and vendors now offer systems with as many as 100 or more individual coil elements. These are applicable to 2D-accelerated time-resolved CE-MRA. Performance is determined by the number of elements available and deployed for a given FOV, their orientation, and the overall SNR they provide.

3D time-resolved CE-MRA has been one of the most successful applications of parallel acquisition in terms of high ($R \geq 4$) acceleration factors being common. This is due to several fundamental factors. First, decomposition of the overall acceleration factor R into individual accelerations, $R = R_Y \times R_Z$, as allowed by the 3D acquisition of CE-MRA, is superior in preserving SNR in the final image vs. performing acceleration R solely along one direction. Second, 3D CE-MRA is typically acquired in coronal or sagittal format with the two phase encode directions transverse (A/P and L/R). Because coil elements can be placed facing each other around the body, these directions are more robust for high acceleration factors than the longitudinal (S/I) direction. Third, MRA images in general, and subtraction CE-MRA images in particular (e.g. Fig. 4f), are sparse, in that the percentage of voxels within the 3D FOV with nonzero signal is small. This reduces the overall signal power and objectionable artifact due to any errors in the mathematical correction for the *k*-space undersampling. Finally, with its increased speed of covering *k*-space, accelerated CE-MRA better maps the high, arterial phase, enhanced signal over the entirety of *k*-space. This provides an overall SNR enhancement effect compared to CE-MRA without acceleration (51) and improved vessel sharpness even with the same sampling resolution as an unaccelerated scan (52). These benefits do not apply when imaging non-time-varying signals. 2D parallel acquisition can likely be further improved by better dispersal of aliasing (53) or parameter optimization on a patient-specific basis (54).

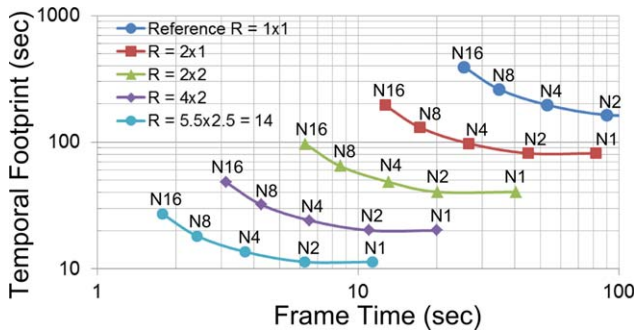

Figure 5. Plot of temporal footprint vs. frame time for different levels of view sharing (N1, N2, etc.) and acceleration (R = 1×1, 2×1, etc.) for 3D CE-MRA of the calves with 1 mm × 1 mm spatial resolution in the 320 × 132 mm^2 FOV of the axial (L/R × A/P) plane. "N" is the number of sectors into which peripheral *k*-space is decomposed as in Fig. 2. N1 corresponds to no view sharing in which case the frame time is equal to the temporal footprint. N2 provides reduced frame time but no increase in footprint. Increased levels of view sharing (N > 2) provide reduced frame time but larger temporal footprint along a given curve. Acceleration R is expressed as $R_Y \times R_Z$. Increased levels of acceleration (larger R) shift the entire curve to smaller frame times and smaller temporal footprints. For this plot the diameter of central *k*-space (the orange zone of Fig. 2a) was 30% of the full *k*-space diameter sampled.

Figure 5 is a plot of temporal footprint vs. frame time for CE-MRA of the calves and shows the dependence of performance on the levels of view sharing and acceleration.

NON-CARTESIAN AND NONTRADITIONAL METHODS

The discussion thus far has focused on Cartesian *k*-space sampling methods. In this section alternative acquisition strategies are considered. There can be a number of fundamental reasons for doing this. Non-Cartesian acquisition strategies such as projection reconstruction (PR) disperse artifacts more uniformly across the image, possibly making them less objectionable than the discrete ghosts characteristic of Cartesian methods. Also, dispersed incoherent undersampling artifact is one of the desired conditions for compressed sensing.

Lauterbur's initial description of MRI in 1973 (55) used PR acquisition, and some of the differentiators of

PR with Cartesian were noted subsequently (56). An early description of PR application to CE-MRA (57) pointed out the relatively benign nature of the artifact in angularly undersampled MRA. This work combined 2D radial sampling in the k_X-k_Y plane with Cartesian sampling in the k_Z direction, a so-called "stack of stars" sampling of *k*-space. Time-resolved CE-MRA results were shown using view sharing. Subsequent work built on this (58–60). Multiple echoes can be sampled per repetition for increased speed in PR (42). Other non-Cartesian *k*-space sampling strategies can be performed in the k_X-k_Y plane such as spiral acquisition (61,62). Rather than the subtle low-signal spoke artifacts of 2D PR, spiral further disperses the artifact in a less coherent fashion due to the further complexity of the spiral trajectory.

PR can be extended to three dimensions (63,64), providing an additional dimension for dispersal of undersampling artifact, potentially allowing greater undersampling than 2D-based PR. One implementation has been dubbed Vastly Undersampled Isotropic Projection Reconstruction, or VIPR. 3D PR is particularly compatible with imaging an FOV that is nominally the same size in all three dimensions, such as the brain. With both 2D and 3D PR the low spatial frequency content associated with the overall image contrast is collected at each projection and allows images to be reconstructed on a projection-by-projection basis, providing considerable flexibility in the specific times, temporal footprints, and spatial resolution for which images in a time series are reconstructed. To best exploit this, the ordering of projections is generally done quasirandomly (65). In contrast to this, the times at which Cartesian-based sampling is reconstructed are linked to the times at which central *k*-space is sampled, as noted in Fig. 3. However, the temporally compact sampling of central *k*-space with centrically ordered Cartesian methods better freezes transient behavior (34).

Almost a decade ago the method of compressed sensing (CS) was described for reconstruction of a function using reduced sampling of its frequencies (66,67) and was first adapted for MRI by Lustig et al (68). CS applied to MRI encompasses a broad framework for performing *k*-space undersampling and image reconstruction, continues to be studied extensively, and a review is beyond the scope of this article. CS techniques can be viewed as another means for acceleration and used synergistically with methods such as view sharing and parallel acquisition. As one example, CS was applied to time-resolved Cartesian acquisitions to restore SNR otherwise lost due to the 20× to 40× acceleration of 2D SENSE and zero filling (69). In another example (70), CS was used with multiecho 3D radial acquisition and a 12-element receiver coil to provide time-resolved images of the brain with the 1-second frame time, an ~100× acceleration vs. unaccelerated Cartesian sampling.

Another approach used for time-resolved acquisition is highly constrained projection reconstruction (HYPR) (71) with variations (72,73). As applied to CE-MRA, this method acquires a high-resolution composite image by sampling the entire or an extended duration of contrast bolus transit. Next, a time series of individually undersampled "raw" frames is formed, typically by subsampling the composite image over short time intervals. Each raw frame is then multiplied by the composite to yield the final time series. This step reduces the artifact level, noise, and blurring characteristic of the individual raw frames. Due to the composite being shared in the formation of each final image, the final image series has image-to-image correlation (74) characteristic of view sharing. Although used extensively with PR, HYPR can also be used with Cartesian sampling (75). In one variant the composite image is formed with one type of sequence, such as noncontrast-enhanced phase-contrast (76) or time-of-flight (77), and the HYPR time frames acquired with a coarsely-sampled, contrast-enhanced run.

MRI OF TIME-VARYING SIGNALS

Time-resolved techniques are generally used in MRA because of the desire to portray the arrival or transit of the contrast-enhanced blood. In the ideal, nonattainable limit, all *k*-space data would be acquired instantaneously at the desired times of imaging. In practice, the mapping of the time-varying signal to *k*-space as dictated by the speed and *k*-space trajectory of the pulse sequence profoundly affects the portrayal of the contrast bolus in the image series. Here, several aspects of this are described.

Consider Fig. 6, taken from Ref. 78, a schematic representation of the arteries in one of the calves. Suppose that contrast-enhanced blood is entering from above the FOV shown, is flowing downward, and has an instantaneously abrupt leading edge. At time $T = 0$ this edge is positioned at level (a), and a time-resolved MRA acquisition is initiated in which all of the central portion and some fraction of the periphery of k_Y-k_Z-space are measured using random sampling similar to Fig. 2c. This is represented in the leftmost *k*-space diagram of the top row. After these data have been accumulated an image is reconstructed. Because not all of peripheral *k*-space has been sampled with contrast present in the vessel, the signal level in the vessel is not at full value and the vessel is not portrayed with full sharpness.

Next assume the process continues: at time $t = T$ the bolus edge has advanced to level "b," and the next cycle of the acquisition is repeated, starting with a second sampling of the *k*-space center followed by a different subset of the periphery. These newly sampled data are used to update the orange central *k*-space of the first image and provide increased peripheral *k*-space sampling, as depicted in the second from left group in the top row. Upon reconstruction this results in improved signal and sharpness in the image at level "a." At level "b," however, the vasculature is portrayed with only one subset of peripheral *k*-space sampled with contrast-enhanced signal, similar to level "a" for time $t = 0$. The process continues for additional cycles until all of *k*-space is fully sampled, yielding full signal and spatial resolution.

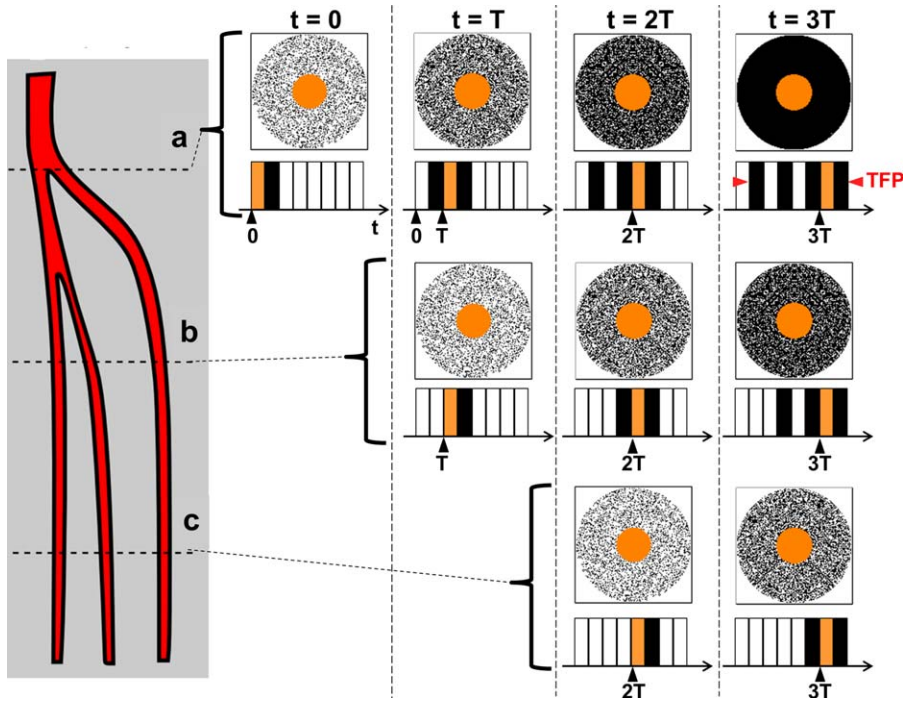

Figure 6. Schematic of the principal arteries of the calf and the degree of *k*-space filling of k_Y-k_Z space at various times for an assumed view-shared acquisition with sampling pattern similar to that in Fig. 2c but with four sectors in peripheral *k*-space. Contrast bolus is assumed to enter from above and steadily progress to levels (**a–c**). Images are reconstructed at times t = 0, T, 2T, 3T. The temporal footprint (TFP) of the sequence is indicated. For additional details see the text.

Figure 7 shows these effects experimentally. In both (a) and (b) the spatial resolution is 1 mm isotropic and the frame time is 2.5 seconds. However, extensive view sharing was used in (a), with eight frame times required before all of *k*-space was fully sampled. In the first few images the vessel edges are blurred and artifacted, and it is only until the fourth or fifth image in the series that the quality approaches that required for diagnosis. A more accelerated acquisition was used in (b) in a different volunteer in which only five frame times were required for complete *k*-space filling. The third or even second image in this series adequately shows the vessels.

These examples show that when the true signal level at a pixel changes over time, it takes several time frames for the signal and spatial resolution in the reconstructed image to "catch up" to the new true level and is a consequence of the sampling of all of *k*-space not being instantaneous. One might attempt to compensate for this by sampling more of peripheral *k*-space after central *k*-space is sampled. However, if an image is ascribed to some time T because that is the time at which central *k*-space is measured, then the use of any data measured after that specific time in forming that image will cause artifactual nonzero signal in blood vessels in advance of the contrast material actually arriving there. This is called "anticipation artifact" and has been described in Cartesian (34) as well as non-Cartesian (79,80) MRA acquisition. A telltale sign is the premature appearance of slight but nonzero signal in venous structures several frame intervals prior to significant enhancement. This can be reduced by reducing the temporal footprint and by sampling central *k*-space near the end of the footprint for any time frame.

Similar effects were observed a decade ago in studies of injection rate (81). For optimum performance the temporal footprint of the MR acquisition approximately matches the duration of high contrast enhancement.

The above considerations can have consequences in depicting a time-varying contrast bolus in blood vessels. Figure 8a shows a plot of a reference curve (blue) in a presumed S/I-oriented enhancing vessel and approximations of this curve as determined from four assumed acquisition techniques. The vessel diameter is relatively large, 32 mm within an assumed 320 (Y) × 132 (Z) mm^2 FOV. A view-shared unaccelerated (R = 1) scan (green) provides the least accurate estimate of the reference. All three other acquisitions provide high fidelity. In (b) a much smaller vessel diameter is assumed, 6 mm. In this case improved match to the reference is evident in going from unaccelerated R = 1 (green) to R = 4 (purple) to R = 8 (cyan) cases. For R = 4, as view sharing is increased from four peripheral *k*-space subsets (N4, purple) to eight (N8, orange), although the frame time is reduced, the fidelity is degraded because the temporal footprint increased per the behavior in Fig. 5. As expected, speeding up any sequence, Cartesian or non-Cartesian, provides improved fidelity in portrayal of the contrast bolus due to reduction of the time necessary to sample all of *k*-space. This is usually traded off with reduced SNR. These and other effects have been studied in detail previously (24,34,79,80,82).

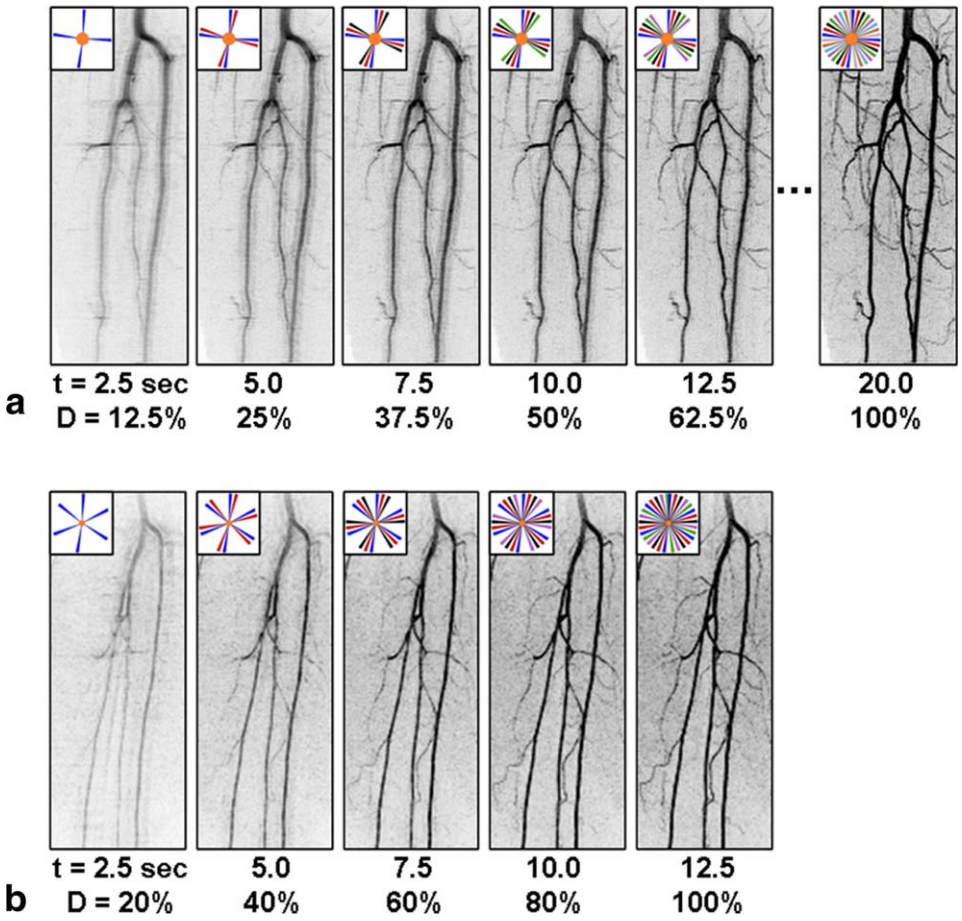

Figure 7. Comparison of the buildup of signal level and spatial resolution in a time-resolved sequence with relatively high level of view sharing (**a**), (N8, 20-second temporal footprint) and moderate view sharing (**b**), (N5, 12.5-second temporal footprint). In both (a,b) the spatial resolution is 1 mm isotropic and the frame time is 2.5 seconds (taken from Ref. 78).

APPLICATIONS

Clinical applications of time-resolved CE-MRA have been widely discussed in the literature. This section provides a sampling of this. The specific application and the choice of time-resolved vs. single phase CE-MRA vs. noncontrast-enhanced MRA vs. use of another modality such as digital subtraction angiography (DSA) or computed tomography angiography (CTA) is highly variable due to both patient-specific factors and radiologist preference.

Head, Neck, and Brain

Imaging of the carotid arteries and the intracranial vasculature is a major application of MRA, and multiple kinds of sequences can be used. Applications of time-resolved CE-MRA include capturing a clear arterial phase of the carotid (25,83–85) and intracranial arteries (24,86–90). Time-resolved acquisitions can simplify existing clinical protocols by avoiding need for a timing bolus (91). Large FOV time-resolved acquisitions of the supraaortic vasculature have been developed for covering the great vessel origins and neurovascular anatomy in a single scan (92–94) but sometimes with a need to reduce A/P coverage or resolution to permit adequate temporal or spatial resolution. Single-phase CE-MRA using 2D SENSE with R = 9 and 16 has been demonstrated using a 16-element coil (95). A common target for time-resolved CE-MRA is to capture the rapid transit of contrast material in arterial-venous malformations (AVMs) (24,33,76,86,96–101), as shown with the HYPR technique in Fig. 9.

Thorax

Imaging the vasculature of the thorax is particularly challenging due to respiratory and cardiac motion. Time-resolved techniques have been used to visualize the transit of contrast material through the pulmonary circulation (102–104). By using a stack of spirals (62) or stack of stars (105) very short, 1.0 second or less, frame times can be achieved. An example of pulmonary imaging is shown in Fig. 10. Time-resolved techniques can also be useful for visualizing the aorta and great vessels (e.g. Ref. 15), and improved thoracic coil designs and parallel imaging strategies have allowed portrayal of perfusion of lung parenchyma over the large FOV (106,107). Another application of time-resolved MRA is the evaluation of congenital cardiovascular disease (108,109), and for pediatric cases; in particular, the exposure-free aspect of MR makes it preferable to CT (110). A low-contrast-dose, time-resolved CE-MRA run (40) can be performed in

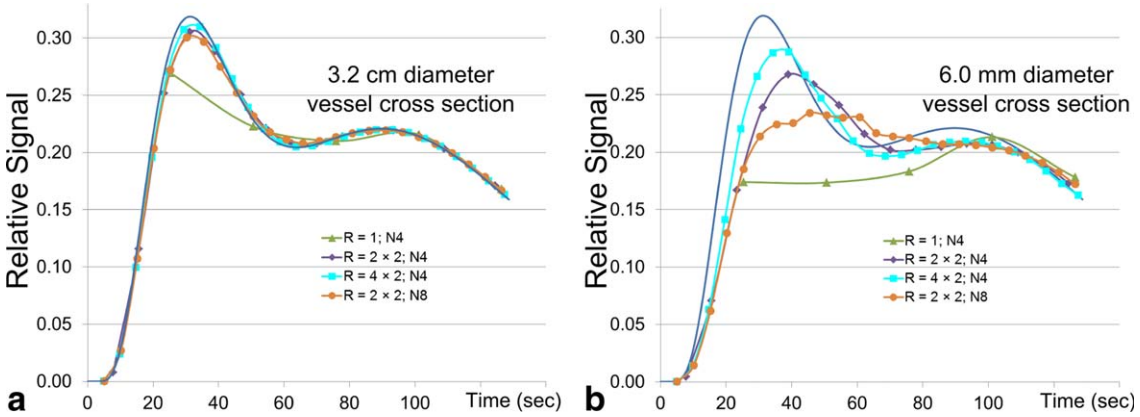

Figure 8. Illustration of temporal fidelity vs. various acquisition strategies for two different assumed vessel diameters for assumed Y × Z FOV of 320 × 132 mm^2. In both **(a,b)** the reference curve, representing actual arterial signal enhancement, is shown in blue. a: Assumed diameter of vessel in the axial (Y-Z) plane is 32 mm. Other than the unaccelerated acquisition (green), all strategies provide a good match of the reconstructed signal with true assumed reference signal. b: Assumed vessel diameter of 6 mm. As acceleration increases from R = 1 to 4 to 8 the match of the reconstructed signal with the reference improves and the frame time also decreases. For fixed acceleration R = 4, as additional view sharing is included, going from N4 (purple) to N8 (orange), although the frame time is reduced, the fidelity decreases owing to the increased temporal footprint.

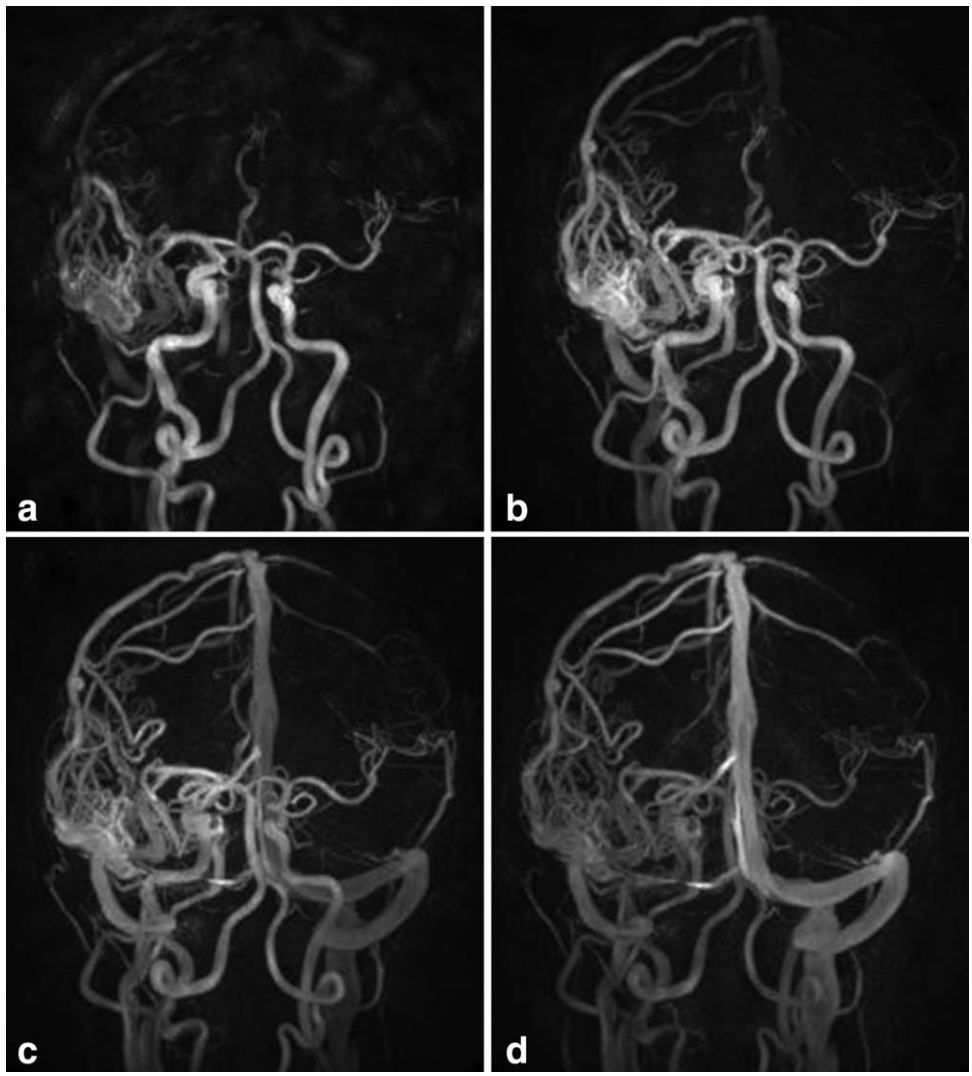

Figure 9. Image of an arteriovenous malformation using the HYPR-Flow method (76) formed from a time-resolved contrast-enhanced run and a 3D phase-contrast-based composite image. Spatial resolution 0.68 mm isotropic, 0.75-second frame time. (Courtesy of Yijing Wu, PhD, Kevin Johnson, PhD, Patrick Turski, MD, and Charles Mistretta, PhD.)

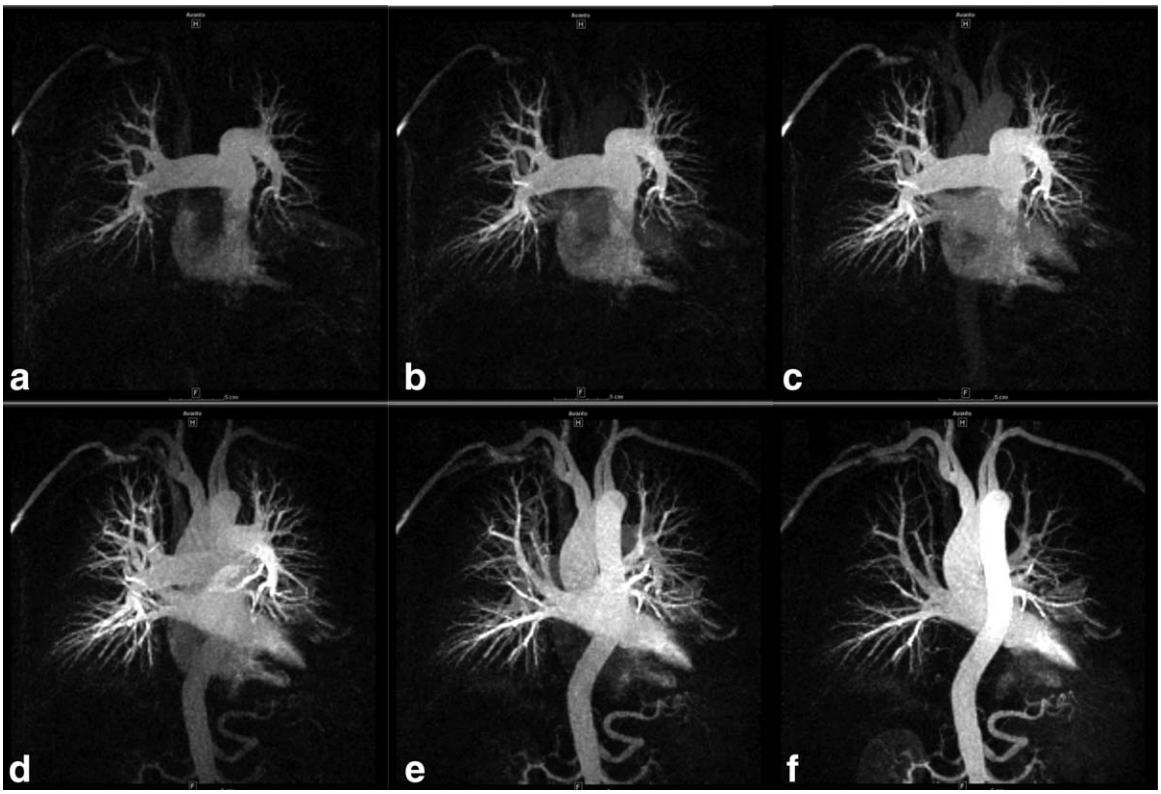

Figure 10. Time-resolved 3D pulmonary CE-MRA acquired using the method reported in Ref. 105. Spatial resolution 1.5 × 1.5 × 3.0 mm^3; 0.7-second frame time. (Courtesy of Timothy J. Carroll, PhD.)

conjunction with a high spatial resolution, single-phase study to provide comprehensive interpretation. An example is shown in Fig. 11.

Abdomen

The abdomen is also a challenging region to image with MR because of respiratory motion and the large FOV. A common study in abdominal MRA is to rule out renal artery stenosis. Noncontrast-enhanced methods (5) have been applied but typically require several minutes of acquisition time. Renal CE-MRA has been an area for application of acceleration techniques for both improved single-phase imaging (111–113) and time-resolved techniques. (37,114) The former can be challenging due to the need for accurate timing. In Ref. 37 the authors adjusted the TWIST sampling to match the anticipated enhancement pattern of the kidney. In Ref. 114 the authors adjusted the CAPR sampling to allow subsecond frame times for timing as well as single phase, high-resolution imaging in a split-dose protocol.

Lower Extremity

In imaging the lower extremity one distinction to be made at the outset is whether the study is limited to a single position or "station" of the patient table or if it requires multiple stations, such as for a complete runoff study. The latter imposes additional technical complexity.

Consider single-station imaging first. Compared to thoracic and abdominal imaging, the lower extremity is less prone to motion artifact. However, timing a single-phase scan after injection is subject to a greater range of delay times due to the distal nature of the vasculature. Also, the proximity of veins to a companion artery makes proper timing to the arterial phase critical. Yet another factor to be sensitive to is the presence of unusual cross-filling or retrograde filling patterns (17,59). Provided the spatial resolution is adequate, time-resolved CE-MRA can well match these factors. As portrayed in Fig. 1, the performance has improved due to many techniques previously identified in this work (14,17,21,22,49,54,64,75,115–118). Acquisition parameters for a number of these recent reports are listed in Table 2, and performance noted in Fig. 12. A number of these works compare CE-MRA with DSA (116,118) or CTA (119).

The proximal vessels of the feet are often included in multistation imaging, but in some instances it may be necessary to focus on one or both feet. A recent review of CE-MRA of the hands and feet (120) described how the improved speed of acquisition has facilitated bilateral FOV, isotropic sub-mm resolution, and frame times of several seconds. Such a study allows distinction of arterial vs. venous vasculature in the presence of differential left vs. right contrast arrival. The improvements in spatial resolution allow improved identification of possible sites of anastomosis for surgery (117,121,122).

Next consider multistation imaging. To keep pace with the advancing contrast bolus from station to

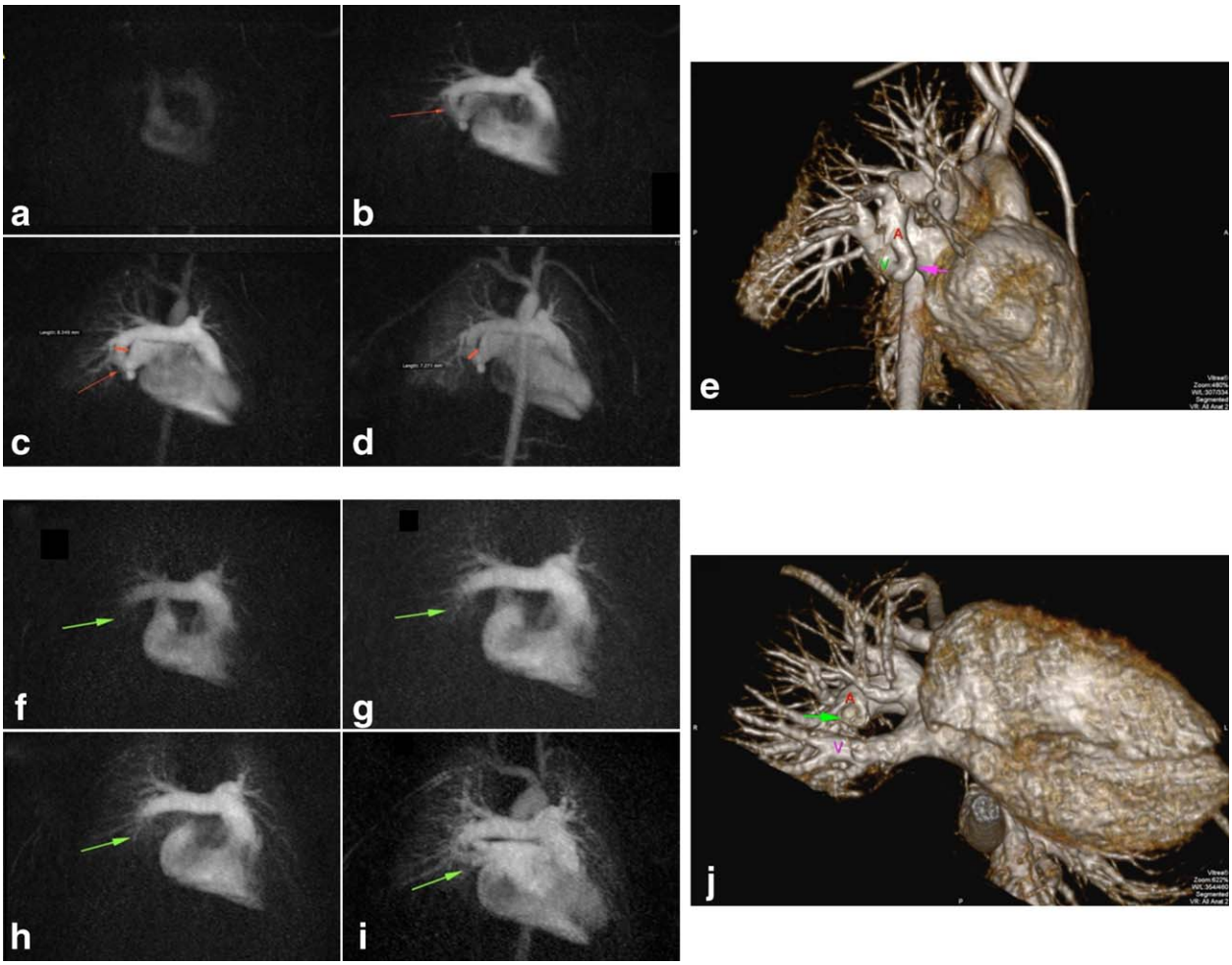

Figure 11. Example of time-resolved CE-MRA of pulmonary arteriovenous fistula of the right lower lobe in a 6-year-old male. **a–d:** Sequence of time-resolved 3D CE-MRA images pretreatment showing the fistula (arrow). Approximate 1-second frame time; 1 ml contrast material. **e:** High-resolution single-phase image showing fistula (red arrow) and the abnormal vascular continuity of the pulmonary artery (A) and vein (V). **f–i:** Sequence of time-resolved images 7 months later, posttreatment, showing normal progression of contrast and absence of fistula. **j:** Companion high-resolution single-phase image confirming occluded fistula (green arrow) and anatomic separation between artery (A) and vein (V). (Courtesy J. Paul Finn, MD.)

Table 2
Summary of Contemporary MRA of the Calves

First Author	Year	Ref.	X (mm)	Y (mm)	Z (mm)	Volume (mm^3)	Frame Time (sec)	Temporal Footprint (sec)
Diehn	2007	116	0.45	0.55	1.00	0.25	28	28
Haider	2009	21	1.00	1.00	1.00	1.00	4.9	19.6
Wu	2009	117	0.80	0.80	1.60	1.02	5.6	89.6
Wu	2009	117	1.70	1.70	3.00	8.67	1.7	27.2
Attenberger	2010	118	1.10	1.10	1.10	1.33	5.49	16
Lim	2010	17	1.00	1.60	1.70	2.72	6.4	18.6
Haider	2010	22	1.00	1.00	1.00	1.00	4.9	4.9
Wang	2011	75	0.94	0.94	1.80	1.59	7.7	69.3
Weavers	2013	54	1.00	1.00	1.00	1.00	3.9	13.8

Performance is shown in Figure 12.

station while still dwelling at an individual station long enough to obtain adequate spatial resolution is technically challenging. Since the initial descriptions of multistation MRA (123,124) considerable effort has been spent to simply get high spatial resolution, single-phase images across the entire FOV (e.g. Refs. 125, 126). Acceleration methods (127,128) and improved coil arrays (49,129) have helped advance

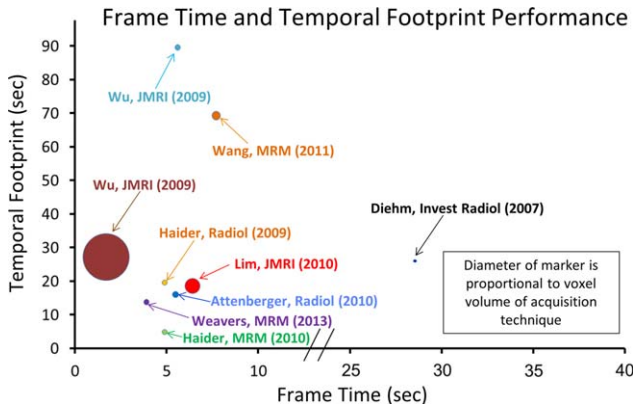

Figure 12. Plot of temporal footprint vs. frame time for time-resolved 3D CE-MRA techniques for imaging the calves listed in Table 2. Diameter of marker for each technique is proportional to the voxel volume of the acquisition. Smaller marker size reflects improved spatial resolution.

this. However, these acquisitions can still be limited with inadequate resolution or venous contamination in the distalmost station. A common way to mitigate this is to use a hybrid approach in which a time-resolved acquisition is done of the calves using a first contrast injection, followed by a dual-station single-phase scan of the abdomen and thighs using a second injection (16,130,131), as illustrated in Fig. 13. Recently, "fluoroscopic tracking" has been described in which a single injection is used, high ($R \geq 8$) acceleration is applied at all stations, 3D images are reconstructed in real time, and table movement is controlled by the operator to match the advancing contrast bolus (38,132).

Upper Extremity

MRA of the hand is a specialized application and also one in which NCE methods have been developed (5). Similar to the feet, the vasculature is relatively distal, making timing uncertain. High spatial resolution is required, and asymmetric left vs. right contrast arrival adds uncertainty. Multielement receiver coil arrays can be devised for this region, allowing high acceleration (120). Recent literature shows how technical performance has been improving (120,133–137), allowing 1 mm^3 acquired resolution and good venous suppression. Applications of time-resolved CE-MRA in the upper extremity include imaging vascular malformations (138) and surveillance of dialysis shunts (139).

DISCUSSION AND SUMMARY

Since its inception almost two decades ago the spatio-temporal resolution of 3D CE-MRA has improved markedly. This advance has been due to increases in the speed of acquisition, as facilitated with improved gradients, reduction of the number of sampled *k*-space points, as allowed with various acceleration methods, and further permitted with view sharing, which allows a frame time shorter than the intrinsic acquisition time of a single frame. However, when taken to an extreme each has its limits, such as degraded SNR, aliasing artifacts, temporal blur, or premature portrayal of contrast arrival.

Perhaps more than any other application in MRI, time-resolved CE-MRA has benefited from the reduced acquisition times allowed by parallel acquisition.

Due to incomplete filling of *k*-space, the first image of a time series portraying contrast arrival in an FOV will generally be subject to less than full signal as well as some loss of spatial resolution. If possible, second and subsequent images should also be used in interpretation.

Although outside the scope of this article, acquisition techniques for time-resolved CE-MRA can be adapted to dynamic contrast-enhanced (DCE) perfusion imaging, and this is an area of growing interest

Figure 13. Radiologic study of the calves. **a:** Still frame from a time-resolved image series showing a stenois in the mid-region of the right anterior tibial artery. **b:** Companion digital subtraction angiography (DSA) result verifying the finding of (a). (Courtesy of Holger Haubenreisser, MD, and Stefan Schoenberg, MD.)

(26,140,141). Time-resolved CE-MRA can be used in many anatomic regions.

ACKNOWLEDGMENT

Contract grant sponsor: NIH; Contract grant numbers: HL070620, EB000212, RR018898.

REFERENCES

1. Prince MR. Gadolinium-enhanced MR aortography. Radiology 1994;191:155–164.
2. Deshmane A, Gulani V, Griswold MA, Seiberlich N. Parallel MR imaging. J Magn Reson Imaging 2012;36:55–72.
3. Tsao J, Kozerke S. MRI temporal acceleration techniques. J Magn Reson Imaging 2012;36:543–560.
4. Grist TM, Mistretta CA, Strother CM, Turski PA. Time-resolved angiography: past, present, and future. J Magn Reson Imaging 2012;36:1273–1286.
5. Miyazaki M, Lee VS. Nonenhanced MR angiography. Radiology 2008;248:20–43.
6. Bernstein MA, Fain SB, Riederer SJ. Effect of zero-filling and windowing of MRI data on spatial resolution and acquisition strategy. J Magn Reson Imaging 2001;14:270–280.
7. Prince M, Narasimham DL, Stanley JC, et al. Breath-hold gadolinium-enhanced MR angiography of the abdominal aorta and its major branches. Radiology 1995;197:785–792.
8. Korosec FR, Frayne R, Grist TM, Mistretta CA. Time-resolved contrast-enhanced 3D MR angiography. Magn Reson Med 1996; 36:345–351.
9. Swan JS, Carroll TJ, Kennell TW, et al. Time-resolved three-dimensional contrast-enhanced MR angiography of the peripheral vessels. Radiology 2002;225:43–52.
10. Weiger M, Pruessmann KP, Kassner A, et al. Contrast-enhanced 3D MRA using SENSE. J Magn Reson Imaging 2000;12:671–677.
11. Sodickson DK, McKenzie CA, Li W, Wolff S, Manning WJ, Edelman RR. Contrast-enhanced 3D MR angiography with simultaneous acquisition of spatial harmonics: a pilot study. Radiology 2000;217:284–289.
12. Chen Q, Quijano CV, Mai VM, et al. On improving temporal and spatial resolution of 3D contrast-enhanced body MR angiography with parallel imaging. Radiology 2004;231:893–899.
13. Weiger M, Pruessmann KP, Boesiger P. 2D SENSE for faster 3D MRI. Magma 2002;14:10–19.
14. Hu HH, Madhuranthakam AJ, Kruger DG, Glockner JF, Riederer SJ. Combination of 2D sensitivity encoding and 2D partial Fourier techniques for improved acceleration in 3D contrast-enhanced MR angiography. Magn Reson Med 2006;55: 16–22.
15. Frydrychowicz A, Bley TA, Zadeh ZA, et al. Image analysis in time-resolved large field of view 3D MR-angiography at 3T. J Magn Reson Imaging 2008;28:1116–1124.
16. Voth M, Haneder S, Huck K, Gutfleisch A, Schoenberg SO, Michaely HJ. Peripheral magnetic resonance angiography with continuous table movement in combination wtih high spatial and temporal resolution time-resolved MRA with a total single dose (0.1 mmol/kg) of Gadobutrol at 3.0 T. Invest Radiol 2009; 44:627–633.
17. Lim RP, Jacob JS, Hecht EM, et al. Time-resolved lower extremity MRA with temporal interpolation and stochastic spiral trajectories: preliminary clinical experience. J Magn Reson Imaging 2010;31:663–672.
18. Bonel HM, Saar B, Hoppe H, et al. MR angiography of infrapopliteal arteries in patients with peripheral arterial occlusive disease by using gadosfosveset at 3.0 T: diagnostic accuracy compare with selective DSA. Radiology 2009;253:879–890.
19. Griswold MA, Jakob PM, Heidemann RM, et al. Generalized autocalibrating partially parallel acquisitions (GRAPPA). Magn Reson Med 2002;47:1202–1210.
20. Noll DC, Nishimura DG, Macovski A. Homodyne detection in magnetic resonance imaging. IEEE Trans Med Imaging 1991;10: 154–163.
21. Haider CR, Glockner JF, Stanson AW, Riederer SJ. Peripheral vasculature: high-temporal and high-spatial-resolution three-dimensional contrast-enhanced MR angiography. Radiology 2009;253:831–843.
22. Haider CR, Borisch EA, Glockner JF, et al. Max CAPR: high resolution 3D contrast-enhanced MR angiography with acquisition times under five seconds. Magn Reson Med 2010;64:1171–1181.
23. Riederer SJ, Tasciyan T, Farzaneh F, Lee JN, Wright RC, Herfkens RJ. MR fluoroscopy: technical feasibility. Magn Reson Med 1988;8:1–15.
24. Haider CR, Hu HH, Campeau NG, Huston J III, Riederer SJ. 3D high temporal and spatial resolution contrast-enhanced MR angiography of the whole brain. Magn Reson Med 2008;60:749–760.
25. Lim RP, Shapiro M, Wang EY, et al. 3D time-resolved MR angiography (MRA) of the carotid arteries with time-resolved imaging with stochastic trajectories: comparison with 3D contrast-enhanced bolus-chase MRA and 3D time-of-flight MRA. Am J Neuroradiol 2008;29:1847–1854.
26. Saranathan M, Rettmann DW, Hargreaves BA, Clarke SE, Vasanawala SS. Differential subsampling with Cartesian ordering (DISCO): a high spatio-temporal resolution Dixon imaging sequence for multiphasic contrast enhanced abdominal imaging. J Magn Reson Imaging 2012;35:1484–1492.
27. Riederer SJ, Bernstein MA, Breen JF, et al. Three-dimensional contrast-enhanced MR angiography with real-time fluoroscopic triggering: design specifications and technical reliability in 330 patient studies. Radiology 2000;215:584–593.
28. Prince MR, Chabra SG, Watts R, et al. Contrast material travel times in patients undergoing peripheral MR angiography. Radiology 2002;224:55–61.
29. Earls JP, Rofsky NM, DeCorato DR, Krinsky GA, Weinreb JC. Breath-hold single-dose gadolinium-enhanced three-dimensional MR aortography: usefulness of a timing examination and MR power injector. Radiology 1996;201:705–710.
30. Wilman AH, Riederer SJ, King BF, Debbins JP, Rossman PJ, Ehman RL. Fluoroscopically-triggered contrast-enhanced three-dimensional MR angiography with elliptical centric view order: application to the renal arteries. Radiology 1997;205:137–146.
31. van Vaals JJ, Brummer ME, Dixon WT, et al. "Keyhole" method for accelerating imaging of contrast agent uptake. J Magn Reson Imaging 1993;3:671–675.
32. Constable RT, Gore JC. The loss of small objects in variable TE imaging: implications for FSE, RARE, and EPI. Magn Reson Med 1992;28:9–24.
33. Petkova M, Gauvrit J, Trystram D, et al. Three-dimensional dynamic time-resolved contrast-enhanced MRA using parallel imaging and a variable rate k-space sampling strategy in intracranial arteriovenous malformations. J Magn Reson Imaging 2009;29:7–12.
34. Mostardi PM, Haider CR, Rossman PJ, Borisch EA, Riederer SJ. Controlled experimental study depicting moving objects in view-shared time-resolved MRA. Magn Reson Med 2009;62:85–95.
35. Wilman AH, Riederer SJ. Performance of an elliptical centric view order for signal enhancement and motion artifact suppression in breathhold three dimensional gradient echo imaging. Magn Reson Med 1997;38:793–802.
36. Willinek WA, Gieseke J, Conrad R, et al. Randomly segmented central k-space ordering in high-spatial-resolution contrast-enhanced MR angiography of the supraaortic arteries: initial experience. Radiology 2002;225:583–588.
37. Song T, Laine A, Chen Q, et al. Optimal k-space sampling for dynamic contrast-enhanced MRI with an application to MR renography. Magn Reson Med 2009;61:1242–1248.
38. Johnson CP, Weavers PT, Borisch EA, et al. Three-station three-dimensional bolus-chase MR angiography with real-time fluoroscopic tracking. Radiology 2014;272:241–251.
39. McGibney G, Smith MR, Nichols ST, Crawley A. Quantitative evaluation of several partial Fourier reconstruction algorithms used in MRI. Magn Reson Med 1993;30:51–59.
40. Finn JP, Baskaran V, Carr JC, et al. Thorax: low-dose contrast-enhanced three-dimensional MR angiography with subsecond

temporal resolution — initial results. Radiology 2002;224:896–904.
41. Madhuranthakam AJ, Hu HH, Barger AV, et al. Undersampled elliptical centric view-order for improved spatial resolution in contrast-enhanced MR angiography. Magn Reson Med 2006;55: 50–58.
42. Jeong HJ, Eddleman CS, Shah S, et al. Accelerating time-resolved MRA with multiecho acquisition. Magn Reson Med 2010;63:1520–1528.
43. Blaimer M, Breuer F, Mueller M, Heidemann RM, Griswold MA, Jakob PM. SMASH, SENSE, PILS, GRAPPA: how to choose the optimal method. Top Magn Reson Imaging 2004;15:223–236.
44. Glockner JF, Hu HH, Stanley DW, Angelos L, King K. Parallel MR imaging: a user's guide. Radiographics 2005;25:1279–1297.
45. Pruessmann KP, Weiger M, Scheidegger MB, Boesiger P. SENSE: sensitivity encoding for fast MRI. Magn Reson Med 1999;42: 952–962.
46. Blaimer M, Breuer FA, Mueller M, et al. 2D-GRAPPA-operator for faster 3D parallel MRI. Magn Reson Med 2006;56:1359–1364.
47. Kellman P, Epstein FH, McVeigh ER. Adaptive sensitivity encoding incorporating temporal filtering (TSENSE). Magn Reson Med 2001;45:846–852.
48. Breuer FA, Kellman P, Griswold MA, Jakob PM. Dynamic autocalibrated parallel imaging using temporal GRAPPA (TGRAPPA). Magn Reson Med 2005;53:981–985.
49. Kramer H, Michaely H, Matschl V, Schmitt P, Reiser M, Schoenberg S. High-resolution magnetic resonance angiography of the lower extremities with a dedicated 36-element matrix coil at 3 Tesla. Invest Radiol 2007;42:477–483.
50. Nael K, Fenchel M, Krishnam M, Laub G, Finn JP, Ruehm S. High-spatial-resolution whole-body MR angiography with high-acceleration parallel acquisition and 32-channel 3.0-T unit: initial experience. Radiology 2007;242:865–872.
51. Riederer SJ, Hu HH, Kruger DG, Haider CR, Campeau NG, Huston J III. Intrinsic signal amplification in the application of 2D SENSE parallel imaging to 3D contrast-enhanced elliptical centric MRA and MRV. Magn Reson Med 2007;58:855–864.
52. Hu HH, Campeau NG, Huston J III, Kruger DG, Haider CR, Riederer SJ. High-spatial-resolution contrast-enhanced MR angiography of the intracranial venous system with fourfold accelerated two-dimensional sensitivity encoding. Radiology 2007;243:853–861.
53. Breuer FA, Blaimer M, Mueller MF, et al. Controlled aliasing in volumetric parallel imaging (2D CAIPIRINHA). Magn Reson Med 2006;55:549–556.
54. Weavers PT, Borisch EA, Johnson CP, Riederer SJ. Acceleration apportionment: a method of improved 2D SENSE acceleration applied to 3D contrast-enhanced MR angiography. Magn Reson Med 2014;71:672–680.
55. Lauterbur PC. Image formation by induced local interactions: examples employing nuclear magnetic resonance. Nature 1973; 242:190–191.
56. Glover GH, Pauly JM. Projection reconstruction techniques for reduction of motion effects in MRI. Magn Reson Med 1992;28: 275–289.
57. Peters DC, Korosec FR, Grist TM, et al. Undersampled projection reconstruction applied to magnetic resonance angiography. Magn Reson Med 2000;43:91–101.
58. Vigen K, Peters D, Grist T, Block W, Mistretta C. Undersampled projection-reconstruction imaging for time-resolved contrast-enhanced imaging. Magn Reson Med 2000;43:170–176.
59. Du J, Carroll TJ, Wagner HJ, et al. Time-resolved, undersampled projection reconstruction imaging for high-resolution CE-MRA of the distal runoff vessels. Magn Reson Med 2002;48: 516–522.
60. Cashen TA, Jeong H, Shah MK, et al. 4D radial contrast-enhanced MR angiography with sliding subtraction. Magn Reson Med 2007;58:962–972.
61. Zhu H, Buck D, Zhang Z, et al. High temporal and spatial resolution 4D MRA using spiral data sampling and sliding window reconstruction. Magn Reson Med 2004;52:14–18.
62. Du J, Bydder M. High-resolution time-resolved contrast-enhanced MR abdominal and pulmonary angiography using a spiral-TRICKS sequence. Magn Reson Med 2007;58:631–635.
63. Barger AV, Block WF, Toropov Y, Grist TM, Mistretta CA. Time-resolved contrast-enhanced imaging with isotropic resolution and broad coverage using an undersampled 3D projection trajectory. Magn Reson Med 2002;48:297–305.
64. Du J, Carroll T, Brodsky E, et al. Contrast-enhanced peripheral magnetic resonance angiography using time-resolved vastly undersampled isotropic projection reconstruction. J Magn Reson Imaging 2004;20:894–900.
65. Winkelmann S, Schaeffter T, Koehler T, Eggers H, Doessel O. An optimal radial profile order based on the Golden Ratio for time-resolved MRI. IEEE Trans Med Imaging 2007;26:68–76.
66. Candes EJ, Rombert J, Tao T. Robust uncertainty principles: exact signal reconstruction from highly incomplete frequency information. IEEE Trans Inf Theory 2006;52:489–509.
67. Donoho DL. Compressed sensing. IEEE Trans Inf Theory 2006; 52:1289–1306.
68. Lustig M, Donaho D, Pauly JM. Sparse MRI: the application of compressed sending for rapid MR imaging. Magn Reson Med 2007;58:1182–1195.
69. Trzasko JD, Haider CR, Borisch EA, et al. Sparse-CAPR: highly-accelerated 4D CE-MRA with parallel imaging and non-convex compressive sensing. Magn Reson Med 2011;66:1019–1032.
70. Lee GR, Seiberlich N, Sunshine JL, Carroll TJ, Griswold MA. Rapid time-resolved magnetic resonance angiography via a multiecho radial trajectory and GraDeS reconstruction. Magn Reson Med 2013;69:346–369.
71. Mistretta CA, Wieben O, Velikina J, Block W, Perry J, Wu Y. Highly constrained backprojection for time-resolved MRI. Magn Reson Med 2006;55:30–40.
72. O'Halloran RL, Wen Z, Holmes JH, Fain SB. Iterative projection reconstruction of time-resolved images using highly-constrained back-projection (HYPR). Magn Reson Med 2008; 59:132–139.
73. Johnson KM, Velikina J, Wu Y, Kecskemeti S, Wieben O, Mistretta CA. Improved waveform fidelity using local HYPR reconstruction (HYPR LR). Magn Reson Med 2008;59:456–462.
74. Keith L, Kecskemeti S, Velikina J, Mistretta CA. Simulation of relative temporal resolution of time-resolved MRA sequences. Magn Reson Med 2008;60:398–404.
75. Wang K, Busse R, Holmes J, et al. Interleaved variable density sampling with a constrained parallel imaging reconstruction for dynamic contrast-enhanced MR angiography. Magn Reson Med 2011;66:428–436.
76. Velikina JV, Johnson KM, Wu Y, Samsonov AA, Turski P, Mistretta CA. PC HYPR flow: a technique for rapid imaging of contrast dynamics. J Magn Reson Imaging 2010;31:447–456.
77. Wu Y, Kecskemeti S, Johnson K, et al. HYPR TOF: time-resolved contrast-enhanced intracranial MR angiography using time-of-flight as the spatial constraint. J Magn Reson Imaging 2011;33: 719–723.
78. Johnson CP, Polley TW, Glockner JF, Young PM, Riederer SJ. Buildup of image quality in view-shared time-resolved 3D CE-MRA. Magn Reson Med 2013;70:348–357.
79. Jeong HJ, Cashen TA, Hurley MC, et al. Radial sliding-window magnetic resonance angiography (MRA) with highly-constrained projection reconstruction (HYPR). Magn Reson Med 2009;61: 1103–1113.
80. Keith L, Rahimi M, Holmes J, Brittain J, Korosec F. Use of a computer-controlled motion phantom to investigate the temporal and spatial fidelity of HYPR processing. Magn Reson Med 2014; 71:702–710.
81. Carroll TJ, Korosec FR, Swan JS, Hany TF, Grist TM, Mistretta CA. The effect of injection rate on time-resolved contrast-enhanced peripheral MRA. J Magn Reson Imaging 2001;14:401–410.
82. Huang Y, Wright GA. Time-resolved MR angiography with limited projections. Magn Reson Med 2007;58:316–325.
83. Golay X, Brown SJ, Itoh R, Melhem ER. Time-resolved contrast-enhanced carotid MR angiography using sensitivity encoding (SENSE). Am J Neuroradiol 2001;22:1615–1619.
84. Carr JC, Shaiban IA, Russell E, Finn JP. Contrast-enhanced magnetic resonance angiography of the carotid. Top Magn Reson Imaging 2001;12:349–357.
85. Ferre J, Brunet J, Carsin-Nicol B, Larralde A, Godey B, Gauvrit J. Optimized time-resolved 3D contrast-enhanced MRA at 3T: appreciating the feasibility of assessing cervical paragangliomas. J Neuroradiol 2010;37:104–108.

86. Meckel S, Mekle R, Taschner C, et al. Time-resolved 3D contrast-enhanced MRA with GRAPPA on a 1.5-T system for imaging of craniocervical vascular disease: initial experience. Neuroradiology 2006;48:291–299.
87. Cashen TA, Carr JC, Shin W, et al. Intracranial time-resolved contrast-enhanced MR angiography at 3T. Am J Neuroradiol 2006;27:822–829.
88. Gauvrit J-Y, Law M, Xu J, Carson R, Sunenshine P, Chen Q. Time-resolved MR angiography: optimal parallel imaging method. Am J Neuroradiol 2007;28:835–838.
89. Willinek W, Hadizadeh D, von Falkenhausen M, et al. 4D time-resolved MR angiography with keyhold (4D-TRAK): more than 60 times accelerated MRA using a combination of CENTRA, keyhole, and SENSE at 3.0T. J Magn Reson Imaging 2008;27:1455–1460.
90. Wu Y, Johnson K, Kecskemeti S, et al. Time resolved contrast enhanced intracranial MRA using a single dose delivered as sequential injections and highly constrained projection reconstruction (HYPR CE). Magn Reson Med 2011;65:956–963.
91. Nael K, Michaely H, Villablanca P, Salamon N, Laub G, Finn J. Time-resolved contrast enhanced magnetic resonance angiography of the head and neck in 3.0 tesla: initial results. Investigative Radiology 2006;41:116–124.
92. Nael K, Villablanca J, Pope W, TO M, Laub G, Finn J. Supraaortic arteries: contrast-enhanced MR angiography at 3.0 T—highly accelerated parallel acquisition for improved spatial resolution over an extended field of view. Radiology 2007;242:600–609.
93. Tomasian A, Salamon N, Lohan D, Jalili M, Villablanca J, Finn J. Supraaortic arteries: contrast material dose reduction at 3.0T high-spatial-resolution MR angiography—feasibility study. Radiology 2008;249:980–990.
94. Lohan D, Tomasian A, Saleh R, Singhal A, Krishnam M, Finn J. Ultra-low-dose, time-resolved contrast-enhanced magnetic resonance angiography of the carotid arteries at 3.0 Tesla. Investigative Radiology 2009;44:207–217.
95. Kukuk GM, Hadizadeh DR, Gieseke J, et al. Highly undersampled supraaortic MRA at 3.0T: initial results with parallel imaging in two direction s using a 16-channel neurovascular coil and parallel imaging factors up to 16. Magn Reson Imaging 2010;28:1311–1318.
96. Ziyeh S, Strecker R, Berlis A, Weber J, Klisch J, Mader I. Dynamic 3D MR angiography of intra- and extracranial vascular malformations at 3T: a technical note. Am J Neuroradiol 2005;26:630–634.
97. Gauvrit J-Y, Leclerc X, Oppenheim C, et al. Three-dimensional dynamic MR digital subtraction angiography using sensitivity encoding for the evaluation of intracranial arteriovenous malformations: a preliminary study. Am J Neuroradiol 2005;26:1525–1531.
98. Hadizadeh DR, Falkenhausen Mv, Gieseke J, et al. Cerebral arteriovenous malformation: Spetzler-Martin classification at subsecond-temporal-resolution four-dimensional MR angiography compared with that of DSA. Radiology 2008;246:205–213.
99. Taschner CA, Gieseke J, Le Thuc V, et al. Intracranial arteriovenous malformation: time-resolved contrast-enhanced MR angiography with combination of parallel imaging, keyhole acquisition, and k-space sampling techniques at 1.5 T. Radiology 2008;246:871–879.
100. Eddleman CS, Jeong HJ, Hurley MC, et al. 4D radial acquistiion contrast-enhanced MR angiography and intracranial arteriovenous malformations. Stroke 2009;40:2749–2753.
101. Hadizadeh DR, Kukuk GM, Steck DT, et al. Noninvasive evaluation of cerebral arteriovenous malformations by 4D-MRA for preoperative planning and postoperative follow-up in 56 patients: comparison with DSA and intraoperative findings. Am J Neuroradiol 2012;33:1095–1101.
102. Fink C, Ley S, Kroeker R, Requardt M, Kauczor H-U, Bock M. Time-resolved contrast-enhanced three-dimensional magnetic resonance angiography of the chest. Invest Radiol 2005;40:40–48.
103. Nael K, Michaely H, Kramer U, et al. Pulmonary circulation: contrast-enhanced 3.0-T MR angiography—initial results. Radiology 2006;240:858–868.
104. Krishnam M, Tomasian A, Lohan D, Tran L, Finn J, Ruehm S. Low-dose, time-resolved, contrast-enhanced 3D MR angiography in cardiac and vascular diseases: correlation to high spatial resolution 3D contrast-enhanced MRA. Clin Radiol 2008;63:744–755.
105. Jeong HJ, Vakil P, Sheehan JJ, et al. Time-resolved magnetic resonance angiography: evaluation of intrapulmonary circulation parameters in pulmonary artery hypertension. J Magn Reson Imaging 2011;33:225–231.
106. Nael K, Fenchel M, Krishnam M, Finn J, Ruehm S. 3.0 Tesla high spatial resolution contrast-enhanced magnetic resonance angiography (CE-MRA) of the pulmonary circulation: initial experience with a 32-channel phased array coil using a high relaxivity contrast agent. Invest Radiol 2007;42:392–398.
107. Attenberger UI, Ingrisch M, Dietrich O, et al. Time-resolved 3D pulmonary perfusion MRI: comparison of different k-space acquisition strategies at 1.5 and 3 T. Invest Radiol 2009;44:525–531.
108. Fenchel M, Saleh R, Dinh H, et al. Juvenile and adult congenital heart disease: time-resolved 3D contrast-enhanced MR angiography. Radiology 2007;244:399–410.
109. Young PM, McGee KP, Pieper MS, et al. Tips and tricks for MR angiography of pediatric and adult congenital cardiovascular disease. AJR Am J Roentgenol 2013;200:980–988.
110. Muthupillai R, Vick GW III, Flamm SD, Chung T. Time-resolved contrast-enhanced magnetic resonance angiography in pediatric patients using sensitivity encoding. J Magn Reson Imaging 2003;17:559–564.
111. Schoenberg S, Rieger J, Weber C, et al. High-spatial-resolution MR angiography of renal arteries with integrated parallel acquisitions: comparison with digital subtraction angiography and US. Radiology 2005;235:687–698.
112. Lum DP, Busse RF, Francois CJ, et al. Increased volume of coverage for abdominal contrast-enhanced MR angiography with two-dimensional autocalibrating parallel imaging: initial experience at 3.0 Tesla. J Magn Reson Imaging 2009;30:1093–1100.
113. Muthupillai R, Douglas E, Huber S, et al. Direct comparison of sensitivity encoding (SENSE) accelerated and conventional 3D contrast enhanced magnetic resonance angiography (CE-MRA) of renal arteries: effect of increasing spatial resolution. J Magn Reson Imaging 2010;31:149–159.
114. Mostardi PM, Glockner JF, Young PM, Riederer SJ. Contrast-enhanced MR angiography of the abdomen with highly accelerated acquisition techniques. Radiology 2011;261:587–597.
115. Thornton FJ, Du J, Suleiman SA, et al. High-resolution, time-resolved MRA provides superior definition of lower-extremity arterial segments compared to 2D time-of-flight imaging. J Magn Reson Imaging 2006;24:362–370.
116. Diehm N, Kickuth R, Baumgartner I, et al. Magnetic resonance angiography in infrapopliteal arterial disease: prospective comparison of 1.5 and 3 Tesla MRI. Invest Radiol 2007;42:467–476.
117. Wu Y, Korosec FR, Mistretta CA, Wieben O. CE-MRA of the lower extremities ujsing HYPR stack-of-stars. J Magn Reson Imaging 2009;29:917–923.
118. Attenberger UI, Haneder S, Morelli JN, Diehl SJ, Schoenberg SO, Michaely HJ. Peripheral arterial occlusive disease: evaluation of a high spatial and temporal resolution 3-T MR protocol with a low total dose of gadolinium versus conventional angiography. Radiology 2010;257:879–887.
119. Young PM, Mostardi PM, Glockner JF, et al. Prospective comparison of Cartesian acquisition withn projection-like reconstruction magnetic resonance angiography with computed tomography angiography for evaluation of below the knee runoff. J Vasc Interv Radiol 2013;24:392–399.
120. Haider CR, Riederer SJ, Borisch EA, et al. High temporal and spatial resolution 3D time-resolved contrast-enhanced MR angiography of the hands and feet. J Magn Reson Imaging 2011;34:2–12.
121. Sharafuddin MJ, Stolpen AH, Shiliang S, et al. High-resolution multiphase contrast-enhanced three-dimensional MR angiography compared with two-dimensional time-of-flight MR angiography for the indentification of pedal vessels. J Vasc Interv Radiol 2002;13:695–702.
122. Ruhl KM, Katoh M, Langer S, et al. Time-resolved 3D MR angiography of the foot at 3 T in patients with peripheral arterial disease. AJR Am J Roentgenol 2008;190:W360–W364.
123. Ho KY, Leiner T, de Haan WM, Kessel AG, Kitslaar PJ, van Engleshoven JM. Peripheral vascular tree stenoses: evaluation with moving-bed infusion tracking MR angiography. Radiology 1998;206:683–692.

124. Meaney JFM, Ridgway JP, Chakraverty S, et al. Stepping-table gadolinium-enhanced digital subtraction MR angiography of the aorta and lower extremity arteries: preliminary experience. Radiology 1999;211:59–67.
125. Leiner T, Ho KY, Nelemans PJ, de Haan MW, van Engleshoven JM. Three-dimensional contrast-enhanced moving bed infusion-tracking (MoBI-Track) peripheral MR angiography with flexible choice of imaging parameters for each field of view. J Magn Reson Imaging 2000;11:368–377.
126. Goyen M, Quick HH, Debatin JF, et al. Whole-body three-dimensional MR angiography with a rolling table platform: initial clinical experience. Radiology 2002;224:270–277.
127. de Vries M, Nijenhuis RJ, Hoogeveen RM, de Haan MW, van Engleshoven JM, Leiner T. Contrast-enhanced peripheral MR angiography using SENSE in multiple stations: feasibility study. J Magn Reson Imaging 2005;21:37–45.
128. Maki JH, Wang M, Wilson GJ, Shutske MG, Leiner T. Highly accelerated first-pass contrast-enhanced magnetic resonance angiography of the peripheral vasculature: comparison of gadofosveset trisodium with gadopentetate dimeglumine contrast agents. J Magn Reson Imaging 2009;30:1085–1092.
129. Fenchel M, Scheule AM, Stauder NI, et al. Atherosclerotic disease: whole-body cardiovascular imaging with MR system with 32 receiver channels and total-body surface coil technology—initial clinical results. Radiology 2005;238:280–291.
130. Wang C-C, Liang H-L, Hsiao C-C, et al. Single-dose time-resolved contrast enhanced hybrid MR angiography in diagnosis of peripheral arterial disease: compared with digital subtraction angiography. J Magn Reson Imaging 2010;32:935–942.
131. Riffel P, Haneder S, Attenberger UI, Brade J, Schoenberg SO, Michaely HJ. Combined large field-of-view MRA and time-resolved MRA of the lower extremities: impact of acquisition order on image quality. Eur J Radiol 2012;81:2754–2758.
132. Johnson CP, Haider CR, Borisch EA, Glockner JF, Riederer SJ. Time-resolved bolus-chase MR angiography with real-time triggering of table motion. Magn Reson Med 2010;64:629–637.
133. Goldfarb JW, Hochman MG, Kim DS, Edelman RR. Contrast-enhanced MR angiography and perfusion imaging of the hand. AJR Am J Roentgenol 2001;177:1177–1182.
134. Brauck K, Maderwald S, Vogt FM, Zenge M, Barkhausen J, Herborn CU. Time-resolved contrast-enhanced magnetic resonance imaging of the hand with parallel imaging and view sharing: initial experience. Eur Radiol 2007;17:183–192.
135. Winterer JT, Moske-Eick O, Markl M, Frydrychowicz A, Bley TA, Langer M. Bilateral ce-MR angiography of the hands at 3.0 and 1.5 T: intraindividual comparison of quantitative and qualitative image parameters in healthy volunteers. Eur Radiol 2008;18:658–664.
136. Winterer J, Blanke P, Schaefer A, Pache G, Langer M, Markl J. Bilateral contrast-enhanced MR angiography of the hand: diagnostic image quality of accelerated MRI using echo sharing with interleaved stochastic trajectories (TWIST). Eur Radiol 2011;21:1026–1033.
137. Andreisek G, Pfammatter T, Goepfert K, et al. Peripheral arteries in diabetic patients: standard bolus-chase and time-resolved MR angiography. Radiology 2007;242:610–620.
138. Mostardi P, Young P, McKusick M, Riederer S. High temporal and spatial resolution imaging of peripheral vascular malformations. J Magn Reson Imaging 2012;36:933–942.
139. Mende KA, Froehlich JM, von Weymarn C, et al. Time-resolved, high resolution contrast-enhance MR angiography of dialysis shunts using the CENTRA keyhole technique with parallel imaging. J Magn Reson Imaging 2007;25:832–840.
140. Wright KL, Seiberlich N, Jesberger JA, et al. Simultaneous magnetic resonance angiography and perfusion (MRAP) measurement: initial application in lower extremity skeletal muscle. J Magn Reson Imaging 2013;38:1237–1244.
141. Xu B, Spincemaille P, Chen G, et al. Fast 3D contrast enhanced MRI of the liver using temporal resolution acceleration with constrained evolution reconstruction. Magn Reson Med 2013;69:370–381.